Ore Geology Reviews 181 (2025) 106634

Contents lists available at ScienceDirect

Ore Geology Reviews

journal homepage: www.elsevier.com/locate/oregeorev

Unsupervised geochemical characterisation of deeply weathered terrains and regolith-hosted REE deposits: Rationale and benefits for exploration

Tobias G. Bamforth [a,b,c,*], Heta M. Lampinen [b], Leah Lynham [d], Nathan Reid [b], Robert Thorne [b], Mario Iglesias-Martínez [b], Joël Brugger [c], Brad Cribb [e], Brett Hazelden [e], Fang Xia [a]

[a] Sustainable Geochemistry and Mineral Sciences, Harry Butler Institute, Murdoch University, Perth, Western Australia 6150, Australia
[b] Commonwealth Scientific and Industrial Research Organisation (CSIRO), Kensington, Western Australia 6151, Australia
[c] School of Earth, Atmosphere & Environment, Monash University, Clayton, Victoria 3800, Australia
[d] College of Science and Engineering, James Cook University, Townsville, Queensland 4810, Australia
[e] OD6 Metals Ltd., Level 1, 50 Kings Park Road, West Perth, Western Australia 6005, Australia

ARTICLE INFO

Keywords:
PCA
K-means
Regolith
REE
Clays
Mineral exploration

ABSTRACT

The accurate characterisation of regolith materials is crucial for mineral exploration, yet distinguishing visually indistinct clay-rich samples can be challenging and labour-intensive. This study conducts unsupervised k-means clustering and principal component analysis (PCA) on a geochemical dataset of over 3000 regolith samples from the Splinter Rock rare earth element (REE) prospect, Western Australia, to determine how unsupervised statistical methods may expedite the characterisation of regolith samples across large, buried and/or regolith-hosted ore deposits. K-means clustering identified five laterally consistent regolith horizons at Splinter Rock, which were manually interpreted into three REE-barren transported horizons and two mineralized saprolite-saprock horizons. The mineralogical and metallurgical features of all 3000 samples were then extrapolated from hyperspectral and metallurgical data of a select few reference samples within their clusters, to provide a preliminary understanding of the deposit's overall structure and properties. Despite being a first-order approach, this method highlighted several consistent, statistically robust and previously unidentified patterns across the entire prospect: 1) the highest REE grades exist predominantly in the granitic saprolite and saprock; 2) relative to the light REEs (La–Sm), the heavy REEs (Eu–Lu) experience enrichment at the saprolite-saprock boundary and depletion with increasing depth in the saprock; 3) optimal metallurgical conditions occur near this saprolite-saprock interface; 4) relative accumulation of the economically- and environmentally-important 'magnet' REEs (MagREE, Pr, Nd, Tb, Dy) occurs mostly in the saprock; and 5) relative MagREE enrichment can be linked to the formation of negative Ce anomalies at lower stratigraphic positions. Lastly, PCA facilitated the development of tailored geochemical ratios to classify future samples into their appropriate horizons. This study highlights unsupervised statistical analysis of existing geochemical data as a robust, rapid and effective first-pass method for classifying and characterising extensive sets of regolith samples, as well as an efficient method of outlining deposit-scale trends and zones of consistent economic REE enrichment in large regolith-hosted deposits/prospects.

1. Introduction

When exploring for mineral deposits within and beneath regolith – the *'entire unconsolidated or secondarily recemented cover that overlies more coherent bedrock, that has been formed by weathering, erosion, transport and/or deposition of the older material'* (Eggleton, 2001) – it is vital that the regolith materials are also well characterised. This is because different materials may: 1) govern geochemical dispersion in different ways, thus dictating what geochemical signatures can be used to find mineral deposits (Anand, 2016; Butt, 2016; Butt et al., 2000; Wang et al., 2016); 2) respond to geophysical surveys in various ways (Caruso et al., 2018; Metelka et al., 2018; Worrall et al., 1998), and; 3) provide different insights into ore formation when mineralisation is regolith-hosted (Johnson and McQueen, 2001; Li et al., 2017; Löhr et al.,

* Corresponding author at: School of Earth, Atmosphere & Environment, Monash University, Clayton, Victoria 3800, Australia.
E-mail address: toby.bamforth@monash.edu (T.G. Bamforth).

https://doi.org/10.1016/j.oregeorev.2025.106634
Received 18 October 2024; Received in revised form 16 April 2025; Accepted 16 April 2025
Available online 16 April 2025

2024), or metal remobilisation when mineralisation is hosted within the underlying bedrock (de Caritat et al., 2017; Henne et al., 2019; Kalinin et al., 2019).

There are, however, several challenges involved when accurately characterising the large numbers of regolith samples that may be collected during mineral exploration campaigns within or beneath cover. Regolith samples are often clay-rich and visually indistinguishable (Anand and Butt, 2010; Arhin and Zango, 2015; Laukamp et al., 2016), such that their classification in large numbers is expected to be time-consuming, labour-intensive, unfocussed (when done without a prior understanding as to the regolith structure, components or influence on mineralisation), and potentially uneconomical where technical methods like X-ray diffraction (XRD) are required for the accurate characterisation of many samples. Furthermore, the potency of these issues is expected to increase as the scale of the exploration area or regolith-hosted deposit increases, which introduces an additional challenge in that the mineralogical, metallurgical and geochemical features of individual samples or drill cores that *are* well-characterised may become increasingly less representative when applied to larger sample sizes.

Given, then, the requirement to uphold global mineral exploration companies that are increasingly employing innovative approaches to mineral exploration in deeply weathered, regolith-dominated terrains (García et al., 2017; González-Álvarez et al., 2020, 2016a; Kelka et al., 2022; Ram et al., 2019; Salama et al., 2016a; Smith et al., 2013; Wang et al., 2016), it is necessary to identify a first-order approach that can help characterise large numbers of regolith samples with a degree of statistical robustness and accuracy. This work thus investigates the efficacy of unsupervised geochemical analyses (i.e., k-means clustering analysis and principal component analysis) as efficient tools by which large numbers of regolith samples can be grouped, defined and used to identify rare earth element (REE, La–Lu, Y, Sc) accumulation patterns at the regolith-hosted Splinter Rock prospect, Western Australia.

Unsupervised geochemical analyses have the benefit of being: 1) widely accessible through industry-standard software (e.g., ioGAS™); 2) applicable to large current and legacy geochemical datasets (Lin et al., 2014), and; 3) rapid, straightforward and tailorable (Bamforth et al., 2022). While this approach can be applied to any regolith setting, it is expected to provide additional value when used to define large regolith-hosted REE deposits. The REEs are widely characterised as critical metals for the development of renewable technologies (Balaram, 2019) and can accumulate in economic concentrations in saprolites and saprocks (i.e., visually indistinct, clay-rich materials) that form during the weathering of granites, granodiorites and volcanic tuffs (Li et al., 2017). Such deposits, however, are low-grade (<0.1 ppm total rare earth oxide, TREO) and high-volume, meaning that it is necessary to define sufficient volumes of mineralised regolith before they can be considered economically viable.

Economic viability depends not only on the REE grade (which must be consistently high in mineralised horizons and may also be sporadically high in unmineralised horizons), but also on REE recovery (which is similarly labour-intensive to define over the necessary numbers of samples). In addition, the geochemical and mineralogical trends that have previously been identified across regolith-hosted REE deposits – which include maximum REE accumulation at the interface between the saprolite (often called the B-Horizon) and saprock (C-horizon) and the relative enrichment of heavy REEs (HREEs, Eu–Lu) with depth in the profile (Li et al., 2017 and references therein) – are rarely (yet necessarily) confirmed to be consistent at the deposit-scale as opposed to the relatively few localised profiles on which these conclusions are based (Bao and Zhao, 2008; Fu et al., 2019; Ichimura et al., 2020; Li et al., 2017; Sababa et al., 2021).

Resultantly, the deposit-scale delineation of sufficiently large regolith horizons that demonstrate acceptable REE accumulation and appropriate metallurgical responses – as well as the validation and extrapolation of previously reported geochemical conclusions over large volumes of regolith – requires the characterisation of over 3000 regolith samples at Splinter Rock. This is conducted herein through their unsupervised geochemical classification. Principal component analysis (PCA) is first applied to identify the chemical elements that mostly govern geochemical variation across all 3000 samples, before these elements are analysed via k-means clustering to group (and hence, visually and volumetrically define) the deposit's individual regolith horizons. The bulk geological and metallurgical natures of each horizon are then interpreted based on their corroboration with regional geology and the extrapolation of their mineralogical, geochemical and metallurgical features that are identified from relatively few reference samples in each cluster (via hyperspectral chip-tray logging and leach tests). Once all clay-rich samples are characterised into their appropriate regolith horizons, conclusions are then made as to the scalability of previously reported geochemical trends in regolith-hosted REE deposits across two different prospects at Splinter Rock (referred to hereafter as Centre and Prop). New insights are then offered into the bulk mechanisms of economically- and environmentally-valuable 'magnet' REE (MagREE, Pr, Nd, Dy, Tb) accumulation in supergene deposits. Lastly, it is shown how PCA results can be repurposed to develop tailored geochemical discriminators, with which future samples can be assigned to their appropriate regolith horizon without having to re-run the analyses.

2. Geological Background

The Splinter Rock prospect resides on the south coast of Western Australia, 130 km to the north-east of Esperance (Fig. 1a). Regional geology comprises two major metamorphic units (the Biranup Zone and Nornalup Zone) which represent lithologies of the adjacent Yilgarn Craton that were reworked throughout the Paleoproterozoic and Mesoproterozoic during the 1815–1800 Ma Salmon Gums Event, the 1780–1760 Ma Ngadju Event, the 1710–1650 Ma Biranup Orogeny and the 1345–1130 Ma Albany-Fraser Orogen (Kirkland et al., 2015, 2011). These events were coeval with the intrusion of various granitic magmas whose compositions evolved over time. Early potassic, calc-alkaline and increasingly ferroan Paleoproterozoic granites of the Biranup Orogeny were superseded by younger alkali-calcic A-type granites that intruded during the Albany-Fraser Orogeny. These include granites of the 1330–1280 Ma Recherche Supersuite and the 1200–1140 Ma Esperance Supersuite (Kirkland et al., 2015). The Splinter Rock prospect sits above granites of the Esperance Supersuite, which split into the Booanya Suite and the Truslove Suite that are dated at 1175 ± 12 Ma and 1196–1135 Ma, respectively (Fig. 1b, Smithies et al., 2015). The Booanya Suite granites are distinguishable from the Truslove Suite by their high K_2O, TiO_2 and P_2O_5 components, and are separable from all other Albany-Fraser granites through their relative REE and high-field-strength element (HFSE) enrichment (Smithies et al., 2015).

Rare earth element accumulation (up to 5000 ppm TREO) is hosted within the lower portions of the Splinter Rock regolith profile, such that these granites might represent the source of REE accumulation (Li et al., 2017). However, the exact nature of the regolith and REE accumulation are unknown; since their emplacement, the Esperance Supersuite granites have been exposed to a range of regolith-forming processes (Anand and Butt, 2010; González-Álvarez et al., 2016b; Salama et al., 2016b). Four main periods of regolith formation in the southern parts of Western Australia are identified after several decades of detailed study (Anand and Butt, 2010; Anand and Paine, 2002 and references therein):

1) *Palaeozoic and Mesozoic Weathering*: Characterised by probable chemical weathering in the Palaeozoic (Pillans, 2005), followed by peneplanation of the West Australian Shield by ice sheets during Gondwanan glaciation (Mory et al., 2008). Glaciation created tunnel valleys and likely formed the Yilgarn Craton and Albany-Fraser drainages (Eyles and de Broekert, 2001; Salama and Anand, 2017). These landforms were then chemically weathered from the late-Permian to the late-Cretaceous under temperate-to-sub-tropical

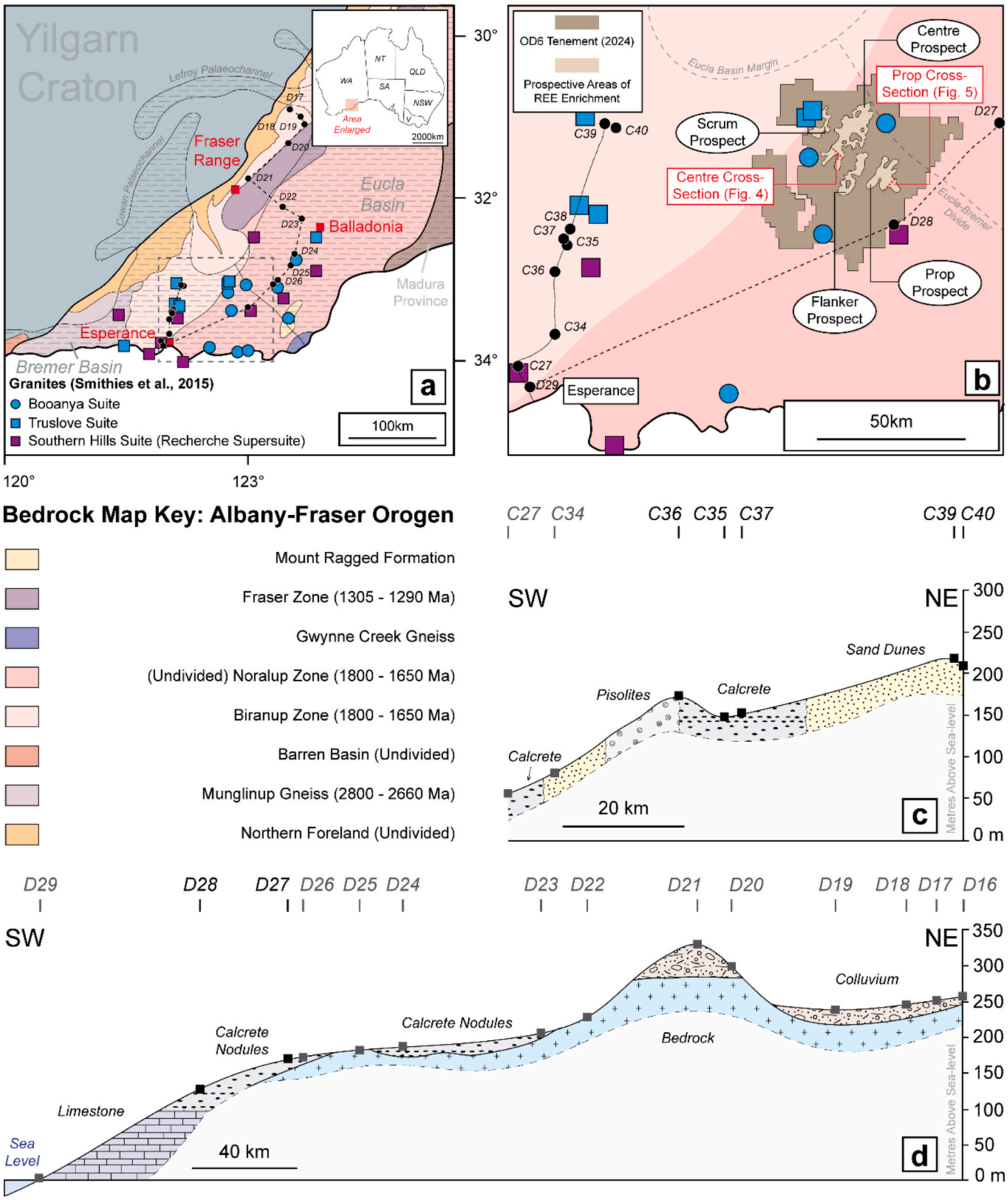

Fig. 1. Geological setting of the Splinter Rock prospect. a) Regional geological units of the Albany-Fraser (A-F) Orogen (modified from Kirkland et al., 2015), overlain by select outcropping granites (Smithies et al., 2015), surface geology transects from González-Álvarez et al., (2016b) and known distributions of transported sediments related to the Eucla and Bremmer basins (Clarke et al., 2003). b) Location of the various Splinter Rock prospects and active OD6 Metals tenement area in relation to these geological features. c and d) Surface transects of sand dunes, calcrete, and colluvium proximal to Splinter Rock (modified from González-Álvarez et al., 2016b). Those laterally consistent with the various prospects are dominated by calcrete and sand dunes (dark markers, text).

conditions, forming saprolite and lateritic residuum on their slopes that merged to ferricrete in the valleys. Palaeomagnetic studies of duricrusts from across parts of the Yilgarn Craton indicate their development during the Jurassic (Embleton, 1981).

2) *Cretaceous to Middle Eocene Erosion*: Characterised by an erosional regime and the deepening of drainage networks by fluvial processes (de Broekert and Sandiford, 2005), following epeirogenic uplift of the Yilgarn Plateau and an increase in stream gradients (de Broekert and Sandiford, 2005).
3) *Mid-to-Late Eocene Sedimentation and Weathering:* Regimes rapidly transitioned from erosional to depositional during the mid-Eocene. Several marine incursions around the study area resulted in the formation of the Eucla Basin and the infill of palaeovalleys by its components; a complex stratigraphic sequence characterised by both high-energy fluvial-estuarine sediments and low-energy marine sediments (Clarke, 1994; Clarke et al., 2003). Since Splinter Rock exists on the onshore Western margin of the Eucla Basin (Fig. 1a), the closest known logs of its palaeovalley infill are those of Eucla Basin sediments around Balladonia and along the Southern coastline (Fig. 2, Clarke et al., 2003). These include early fluvial-estuarine gravels, clays and lignite-rich layers of the Werrilup Formation, as well as the subsequent glauconite-rich marine sediments of the Pallinup Formation (Fig. 2a). Further south-west towards the modern-day coastline, the North Royal Formation and the Nanarup Limestone are also recognised to have pre-dated the Werrilup Formation (Fig. 2b). A warm and wet climate during the mid-to-late Eocene is indicated by palynofloral assemblages that include rainforest taxa (Carpenter and Pole, 1995; Itzstein-Davey, 2004). Late-Eocene weathering is thus characterised by seasonally humid subtropical-to-tropical conditions, which affected bedrock and the transported sediments (Anand and Butt, 2010). However, since most of the sedimentary infill is not deeply weathered, the majority of deep chemical weathering in the region is suggested to have occurred during the Mesozoic, rather than the Eocene period (Anand and Paine, 2002; Eyles and de Broekert, 2001; Salama and Anand, 2017).
4) *Post Eocene Sedimentation and Weathering*: Characterised by the onset of aridity resulting from the formation of the Antarctic Circumpolar Current (ACC), tectonic uplift in the southwest, the rejuvenation of river systems and the return of erosional processes (Anand and Butt, 2010). Erosional products were transported and deposited as colluvial, alluvial and aeolian sediments. Some regolith units become cemented by Fe-oxides, silica, aluminosilicates and/or carbonates. These arid conditions resulted in the drying of the drainage systems that traversed Western Australia (Clarke, 1994; Van de Graaff et al., 1977), leading to chains of salt lakes and the formation of associated gypsum and dune deposits. Today the drainage systems contain hypersaline ground waters, >95 % of which is from marine inundation of the Yilgarn Craton (De Silva and Smith, 2010). The drainage systems often become active again at the surface following periods of heavy rainfall.

Combined, these processes resulted in the development of a complex regolith profile across the Yilgarn Craton and Albany-Fraser Orogen (Anand and Butt, 2010; Clarke et al., 2003). Near Splinter Rock, the surface expression of this profile is characterised by Fe-pisolites, sand dunes and occurences of calcrete (either pedogenic or following limestone weathering) that are standalone or associated with those dunes (Fig. 1c and d, González-Álvarez et al., 2016b). There is little evidence as to the nature of local regolith material beneath these shallow horizons, such that the regional regolith framework described is applied only to loosely contextualise the chemostratigraphic horizons that are identified.

Furthermore, the exact nature of REE accumulation at Splinter Rock is currently undergoing detailed investigation (Reid et al., in review), though based off preliminary investigations (Sergeev and Collins, 2024) it is believed to relate to the precipitation of secondary REE minerals like rhabdophane (i.e., Bamforth et al., 2024b), rather than the adsorption of REEs onto clays, during saprolite formation. This may make Splinter Rock either different or similar to the Chinese ion adsorption type deposits that are refferenced throughout this paper (Trench et al., 2024),

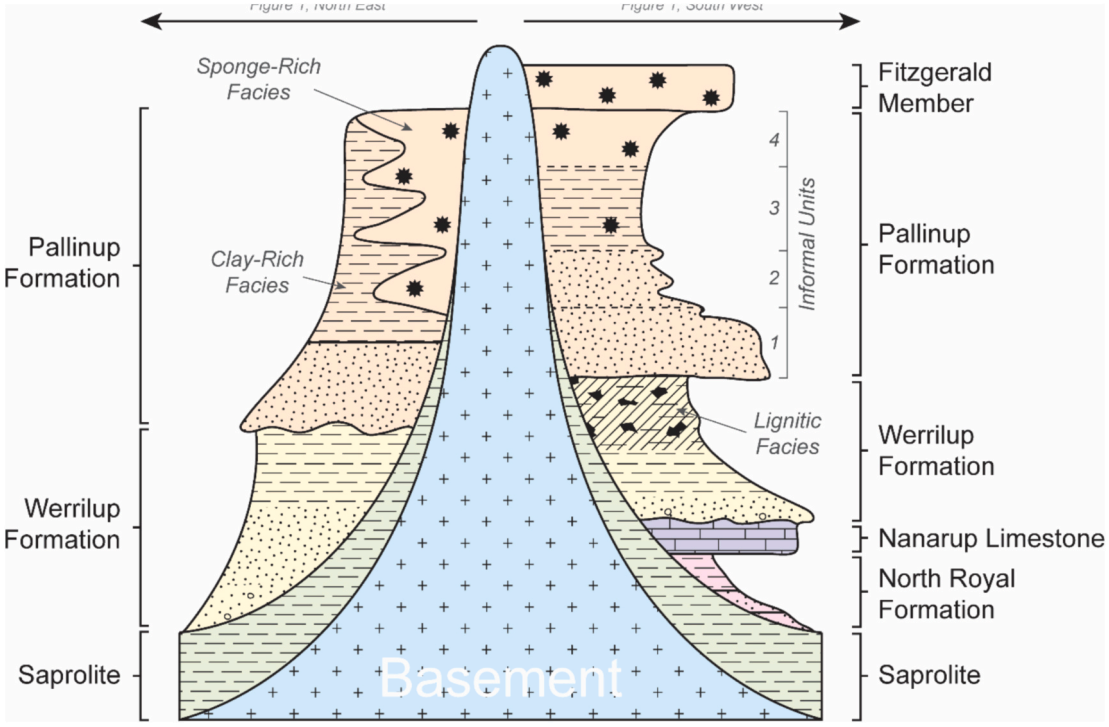

Fig. 2. Reported variations in the regolith framework either side of the Splinter Rock prospect, from the Balladonia region in the Northeast to the Southern coastline. Modified after Clarke et al. (2003). Notable features include the lignitic facies which forms part of the upper Werrilup Formation towards the coast, as well as the numerous clay-rich transported sediment layers which overly (and are mineralogically similar to) the saprolite.

though in the case of the fomer fundemental differernces in terms of REE behaviours during weathering (and the applicability of the approach described herein to different types of regolith-hosted REE accumulation) are not expected.

3. Methods

3.1. Sampling and assaying

This study focuses on two of the four prospective areas at Splinter Rock – Centre and Prop (Fig. 1b) – and is based on 1083 and 2185 whole rock analyses, respectively. Samples were obtained via air core drilling at depths between 0 and 108 m (Electronic Supplementary Material). Composite assays of the resulting chip materials were collected over 3 m intervals and represent 9804 m of drilling. All drilling was conducted at 0° such that the samples represent simple cross-sections through the regolith profile.

Each sample was routinely assayed for 60 elements (Ag, Al, As, Ba, Be, Bi, Ca, Cd, Ce, Co, Cr, Cs, Cu, Dy, Er, Eu, Fe, Ga, Gd, Ge, Hf, Ho, In, K, La, Li, Lu, Mg, Mn, Mo, Na, Nb, Nd, Ni, P, Pb, Pr, Rb, Re, S, Sb, Sc, Se, Sm, Sn, Sr, Ta, Tb, Te, Th, Ti, Tl, Tm, U, V, W, Y, Yb, Zn, Zr) by four-acid (HF-HNO_3-$HClO_4$-HCl) digest and inductively coupled plasma (ICP) atomic emission spectroscopy (AES) and mass spectroscopy (MS) finishes at Australian Laboratory Services (ALS), Perth (analysis code ME-MS61r). All elements were measured by ICP-AES, whereas four (Bi, Mo, Ag and W) were re-analysed by ICP-MS. The detection limits and full dataset can be found in the Electronic Supplementary Material (ESM). During analysis, rigorous quality assurance and quality control (QA/QC) was ensured. Field-introduced checks included: 1) duplicate checks (approximately 1 per 59 samples); 2) confirmation analyses of certified reference materials (approximately 1 per 37 samples), and; 3) blank checks (approximately 1 per 79 samples).

3.2. Application and calculation of Ce anomalies, Eu anomalies and lambda values

To avoid collinearity issues during K-means analysis and PCA (Dormann et al., 2013), the highly co-dependent REEs were not included as fourteen unique variables. Rather, the contribution of the REEs to geochemical variance was assessed by their representation through six independent variable groups: 1) total rare earth oxide (TREO) concentrations; 2) relative 'magnet' rare earth element (MagREE) percentages; 3) cerium anomalies (Ce/Ce*); 4) europium anomalies (Eu/Eu*); 5) lambda 1 values (λ1), and; 6) Y/Ho ratios. The descriptions and calculations for each are found in Table 1. Values of Ce/Ce*, Eu/Eu* and λ1 (broadly equivalent to LREE/HREE) were calculated using the web application BLambdaR (output version 2022–01-05, accessed 09–11-2023) which employs the polynomial fitting methods given in O'Neill (2016) and Anenburg and Williams (2022). Cerium anomalies (Barrat et al., 2023) are of particular interest in regolith profiles, since they evidence oxidising formation conditions (i.e., weathering, sedimentary deposition) where the oxidation of Ce (III) to Ce (IV) results in the in-situ uptake of Ce into minerals like cerianite and hematite, limited downwards mobilisation of Ce relative to the remaining REEs and the subsequent formation of positive and negative Ce anomalies at the tops and bottoms of weathering profiles, respectively (Braun et al., 1990; Ichimura et al., 2020). They are included and discussed throughout this paper to provide additional context on regolith development.

3.3. Geochemical data scrubbing

In preparation for statistical analysis, the whole-rock geochemical datasets from Centre and Prop were scrubbed following the methodology of Hood et al. (2019). Zero values (i.e., values that were below the limit of detection, LOD, of ICP-MS and ICP-AES analysis) were first replaced by values equal to 50 % of LOD in variables where the number

Table 1
Descriptions and equations for abbreviations of element ratios and indices used in this paper.

Abbreviation	Extended	Description	Calculation	Reference
TREO	Total Rare Earth Oxide	Total grade of all REEs, La – Lu	ΣREE (La – Lu)	–
LREE	'Light' Rare Earth Element	Total grade of the 'light' REEs, La – Sm	ΣREE (La – Sm)	–
HREE	'Heavy' Rare Earth Element	Total grade of the 'heavy' REEs, Eu – Lu	ΣREE (Eu – Lu)	–
MREE	'Middle' Rare Earth Element	Less common subdivision of 'middle' REEs, Sm – Dy	ΣREE (Sm – Dy)	–
MagREE (%)	Relative Magnet Rare Earth Element Enrichment (%)	Relative percentage of REEs that are used to produce permanent magnets for renewable technologies.	((Pr, Nd, Dy, Tb)/ TREO)*100	This Study
Ce/Ce*	Cerium Anomaly	Position of Ce on a chondrite normalised REE profile, relative to a linear/ polynomial extrapolation between La and Nd (Ce*).	See Specific Reference	Linear Extrapolation: Barrat et al., (2023) Polynomial Extrapolation: O'Neill (2016)
Eu/Eu*	Europium Anomaly	Position of Eu on a chondrite normalised REE profile, relative to a linear/ polynomial extrapolation between Sm and Gd (Eu*).	See Specific Reference	Linear Extrapolation: Barrat et al., (2023) Polynomial Extrapolation: O'Neill (2016)
λ1	Lambda 1	Linear slope of a chondrite normalised REE profile, when fitted to a polynomial function. Larger values indicate greater LREE enrichment.	See Specific References	Theory: O'Neill (2016) Calculation: Anenburg and Williams (2022)
CIA	Chemical Index of Alteration	Whole-rock proportions of *immobile* Al (found in secondary clay minerals) relative to *mobile* metals (Ca, Na, K, found in unweathered primary minerals like feldspars and olivines).	(Al_2O_3/ (Al_2O_3 + CaO + Na_2O + K_2O))*100	Nesbitt and Young (1982)
TMI	Transported Metal Index	Relative proportions of site-specific transported elements (As,	((As + Cr)/ (As + Cr + P + Ba)) *100	This Study

(*continued on next page*)

Table 1 (*continued*)

Abbreviation	Extended	Description	Calculation	Reference
		Cr) relative to site-specific in-situ elements (P, Ba).		
WEI	Weathering Enrichment Index	Relative proportions of site-specific 'weathering depleted' elements (Ca and K) relative to site specific 'weathering enriched' elements (S and Zr).	((Ca + K)/(Ca + K + S + Zr))*100	This Study

of zero-value observations was <33 % of the total number of observations (Carranza, 2011). From the Centre dataset, these variables were As, Ca, Ge, Sb, Tm and Lu (the LODs of which, in ppm, were 0.2, 100, 0.05, 0.05, 0.1 and 0.1, respectively). From the Prop dataset, these variables were As, Ba, Cs, Ge, In, P, S, Sb, Zn, Tb, Tm and Lu (the LODs of which, in ppm, were 0.2, 10, 0.05, 0.05, 0.05, 10, 100, 0.05, 2, 0.1, 0.1 and 0.1 respectively). For the REEs Tb, Tm and Lu, these values were replaced before being included in calculations of the independent variables that are discussed above, and were not included in the analysis individually. Observations with zero values require replacement since the log-ratio transformations applied to compositional datasets prior to multivariate analysis cannot be applied to zero values (Aitchison, 1982). A centred-log ratio was then applied to the dataset using the CoDaPack (v.2.03.01) freeware (Thió-Henestrosa and Martín-Fernández, 2005). Finally, other highly co-dependent variables ($r^2 > 0.85$) were determined in both datasets by correlation analysis of the transformed data and were excluded from statistical analysis. These were Hf, Rb, Ta and Sn, which are co-correlated with Zr, K, Nb(+Sn) and Nb(+Ta), respectively.

3.4. Principal component analysis and k-means clustering

All of the remaining elements were included in PCA, so as to: 1) map their associations with each other and the resulting k-means clusters; 2) best determine the 'real-world' geological controls on the PCs, and; 3) accurately assign the clustered layers to regional regolith horizons based partly on their complete chemistry. The statistical and clustering analyses followed a PCA-to-k-means workflow (Hood et al., 2019). Firstly, PCA was conducted to define which of these variables (elements) govern the largest degree of variance across each geochemical dataset from Centre and Prop. To do this, Classical PCA was conducted on a covariance matrix of the above-transformed data using the XLSTAT™ plugin (v 2021.1.1.1073) for Microsoft Excel 365. The results (Electronic Supplementary Material, ESM) identified different variables (26 at Centre and 32 at Prop) for which the squared cosine is largest in either principal component (PC) 1 or PC2 (i.e., whose predominant contribution to the geochemical variance was as part of the two largest drivers of variance). For the sake of consistency, all the variables that contributed mostly to PC1 or PC2 at *either* Centre or Prop were included in the final list of 33 variables, which were then subject to the k-means analysis (ESM 1). K-means was selected as the preferred clustering method due to its ease of use and speed when analysing large datasets, and was run in XLSAT for between 1 and 10 clusters (K) using a function trace clustering criterion based on the Euclidian distance method (Krzanowski and Lai, 1988). The initial partition was set to random, with the stop conditions set to 20 iterations and a convergence of 0.00001. Finally, the resulting k-means clusters were imprinted back onto the observations that were included in the PCA analysis, so as to contextualise the PCA results that subsequently allow for the geochemical classification of each cluster.

3.5. Hyperspectral mineralogy

Infrared reflectance spectra from chip trays of two drill holes from Splinter Rock were collected using the CSIRO Geoscience Drill Core Research Laboratory's HyLogger-3™ system. The HyLogger-3 system chip mode simultaneously collects high-resolution (0.1 mm pixel) digital colour photographs – as well as three infrared reflectance spectra over the visible-to-near-infrared (VNIR: 380–1300 nm), short-wave infrared (SWIR: 1300–2500 nm) and thermal infrared (TIR: 6000–14500 nm) wavelength ranges – at 1 m chip bucket intervals. These spectra are then averaged into one high-quality spectrum. The technical aspects of HyLogger-3 data acquisition are described in Schodlok et al., (2016). Data were processed using The Spectral Geologist (TSG™, research.csiro.au/thespectralgeologist) software to determine a mineral's presence, abundance, and composition. Individual drill hole TSG files were merged into one file to ensure consistent processing. HyLogger-3 data are automatically processed by The Spectral Assistant (TSA) linear unmixing algorithm within the TSG software (Berman et al., 2017). This compares the experimental infrared reflectance spectra against three in-built mineral spectral reference libraries (SRLs) and identifies several possible minerals based on the fit. System-generated matches are visually compared against the in-built SRLs to vet erroneous matches. Erroneous matches are turned off and the TSA algorithm is re-run for confirmation. The diagnostic infrared reflectance spectral features for the final minerals of interest were then investigated using both single and/or multiple feature targeting algorithms as described in Laukamp et al. (2021). The mineral indices of interest (and their previously published scripts as applied) were: 1) kaolin abundance and crystallinity (Sonntag et al., 2012); 2) ferric oxide abundance and composition (Haest et al., 2012a, 2012b); 3) smectite abundance and Al-clay composition (i.e., kaolinite vs. Al-smectite), based on water absorption at 1900 nm wavelength (Doublier et al., 2010), and; 4) quartz abundance (Laukamp et al., 2021).

3.6. Metallurgical tests

At Splinter Rock, OD6 Metals has employed an acid leach approach to extracting economically viable concentrations of REEs from their low-grade, high-tonnage deposit (OD6 Metals Ltd, 2024). To discuss how the metallurgical results of this approach vary between the k-means clusters, metallurgical test results that were previously reported on the Australian Stock Exchange (ASX) are assigned to the clusters now associated with those samples. The method of metallurgical testing is described herein.

At the Australian Nuclear Science and Technology Organisation (ANSTO), the regolith samples were first air-dried at 50 °C before being crushed and screened to 1 mm passing. The samples were then split in half, with one half being used for the head assay and the other being used for metallurgical tests. The head assay was measured by X-ray fluorescence (XRF) at ANSTO for the gangue elements Al, Ca, Fe, K, Mg, Mn, Na and Si, and by four acid digest with ICP-MS finish at the Australian Laboratory Services (ALS) geochemistry laboratory in Brisbane for trace REE, U, Th and Sc. The metallurgical tests were conducted at ANSTO by leaching 40 g of dry, pulverised sample with 1960 g of lixiviant (25 g/L HCl in water) for 24 h at 30 °C. Tests were conducted in baffled glass leaching vessels equipped with overhead stirrers, in which the acidity was monitored regularly by undertaking free acid titrations of liquors that were sampled every three hours (i.e., thief samples). Upon completion, the solids were recovered by vacuum filtration, washed thoroughly with 100 ml of deionised water and dried at 50 °C. The chemistries of the final and thief liquors were analysed for the REEs, Th and U by ICP-MS at ALS, and for the gangue elements above by ICP-OES at ANSTO. Lastly, the chemistries of the final leach solids were also analysed for these elements via the methods described above for the head assays.

Final element and REE recoveries from each sample were calculated using the head and leach residual compositions, combined with their sample weights before and after digestion through Eq. (1):

$$\frac{[HS_w \times HS_a] - [SR_w \times SR_a]}{HS_w \times HS_a} \quad (1)$$

where HS_w is the head sample weight, HS_a is the HS assay, SR_w is the solid residue (SR) weight and SR_a is the SR assay. Acid consumption during the reaction of samples was calculated by: 1) determining the number of moles of pH-buffering gangue elements (Al, Ca, Fe, Si, Mg and Na) in the final liquor volume via its assay; 2) stoichiometrically calculating the number of moles of HCl consumed by each of these elements; 3) converting those moles to grams of HCl, and; 4) referencing that value to the initial sample mass to get the number of kilograms of acid consumed for every tonne of sample.

4. Results

4.1. K-means clustering

The within cluster variance results (Fig. 3a) and silhouette scores (Fig. 3b) of K-means analyses ($K \leq 10$) for both prospects were used to determine the 'optimal' number of clusters. From this, $K = 5$ was selected as this optimal number, as in both prospects this represented the inflection point in Fig. 3a (i.e., lowest optimal within-cluster variance) and an optimal peak in Fig. 3b (i.e., the highest optimal between cluster variance). When the drill cores and their resulting clusters are mapped into cross sections of the Centre prospect (Fig. 4) and Prop prospect

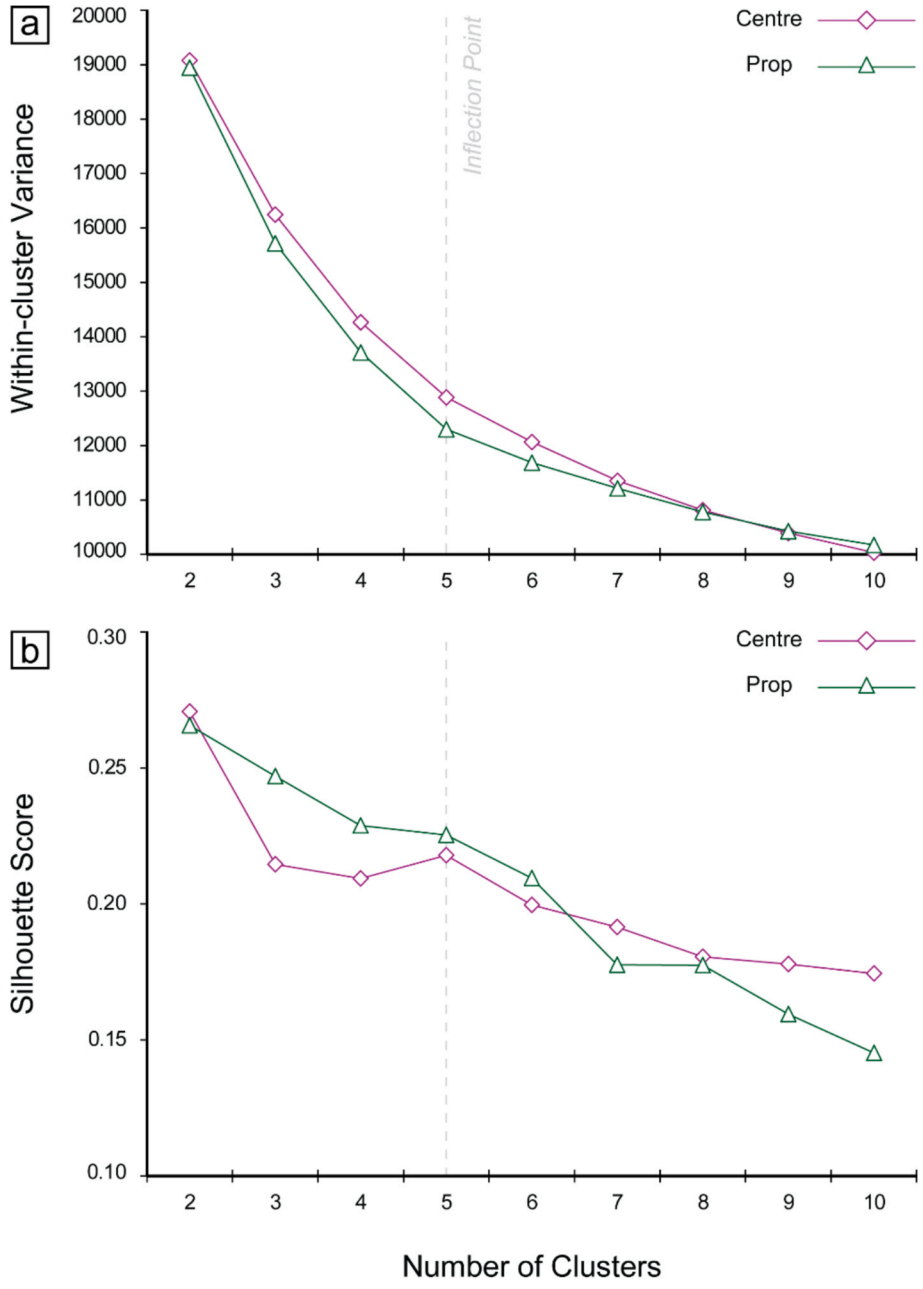

Fig. 3. K-means clustering results of geochemical assays sampled from the Centre prospect (n = 1083) and Prop prospect (n = 2185). The inertia (i.e., within-cluster variance, a) indicates the extent of data separation within each of the clusters, such that smaller values indicate good separation. The silhouette score (b) indicates the extent of separation between each of the clusters, such that higher values indicate good separation. Based on these results, five clusters were chosen as the 'optimal' number for each dataset, since five clusters represents the inflection point in inertia (a) and offers acceptably large silhouette scores (b) relative to four or six clusters.

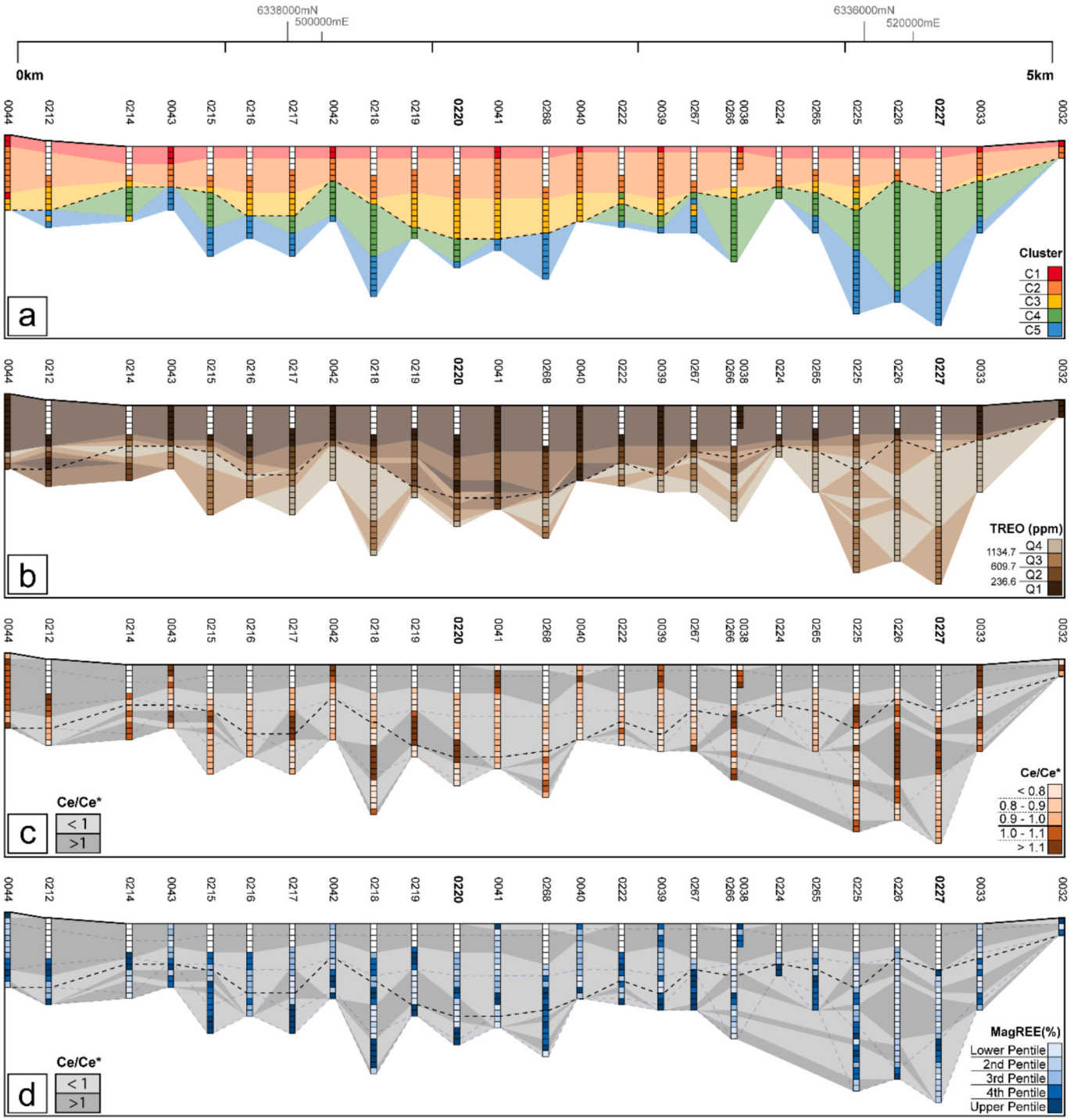

Fig. 4. Geochemical cross-sections across the Centre prospect, with each square representing a 3 m sampling interval. a) Clusters defined from K-means clustering analysis. Note the overall stratigraphic consistency that derived from unsupervised analysis. b) Total rare-earth oxide (TREO) values (in ppm), mapped by their quartiles (Q1–Q4). c) Cerium anomaly values, with dark values representing positive Ce anomalies and light values representing negative Ce anomalies. d) Magnet REE (MagREE) percentages, mapped by their pentiles (with the upper pentile representing the highest MagREE percentages). Note the general association between stratigraphic sections of high MagREE percentages (dark blue) and those with negative Ce anomalies (light grey). Dark dashed line represents the interpreted boundary between transported materials (above, C1–C3) and in situ sediments (below, C4–C5). Faint dashed lines represent the boundaries for each of the Clusters given in (a). (For interpretation of the references to colour in this figure legend, the reader is referred to the web version of this article.)

(Fig. 5), they present as laterally dependable chemostratigraphic horizons that are consistent relative to each other and between prospects. Of further interest to these cross sections are the extents of REE enrichment associated with each chemostratigraphic horizon (Figs. 4b and 5b as grouped into quartiles (Q1–Q4) calculated from all datapoints within that prospect), their variations in Ce anomalies with depth (Fig. 4c and 5c) and their relative MagREE contributions (Figs. 4d and 5d) that are discussed in detail later in the paper.

4.2. Principal component analysis

The five clusters from Centre (Fig. 6a) and Prop (Fig. 6b) were

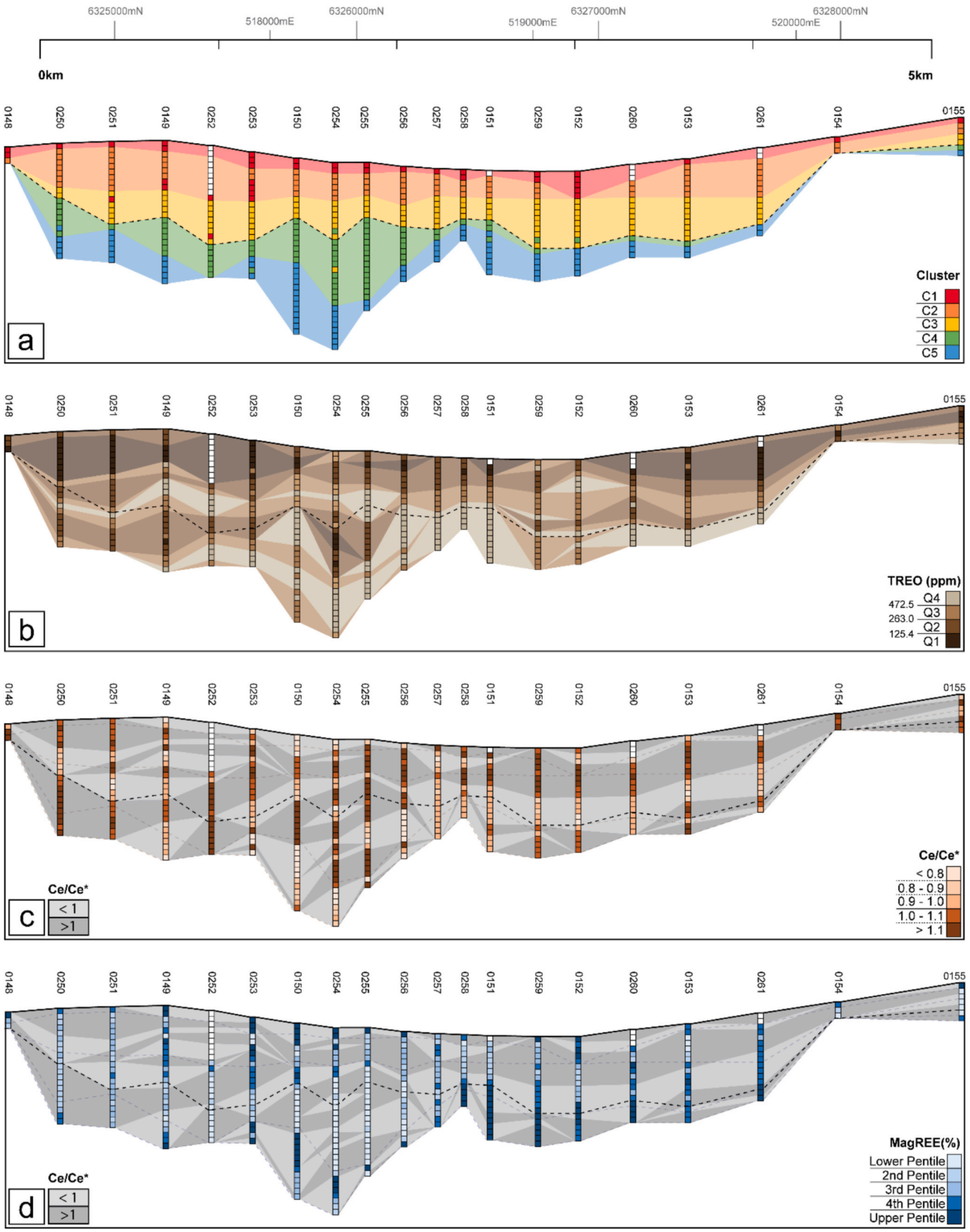

Fig. 5. Geochemical cross-sections across the Prop prospect, with each square representing a 3 m sampling interval. a) Clusters defined from K-means clustering analysis. b) Total rare-earth oxide (TREO) values. c) Cerium anomaly values. d) Magnet REE (MagREE) percentages, mapped by their pentiles. While certain horizons exhibit a similar correlation between Ce anomalies and MagREE enrichment as is prevalent in the Centre prospect (Fig. 4), MagREE percentages in the Prop prospect appear more reliant on the geochemical cluster boundaries.

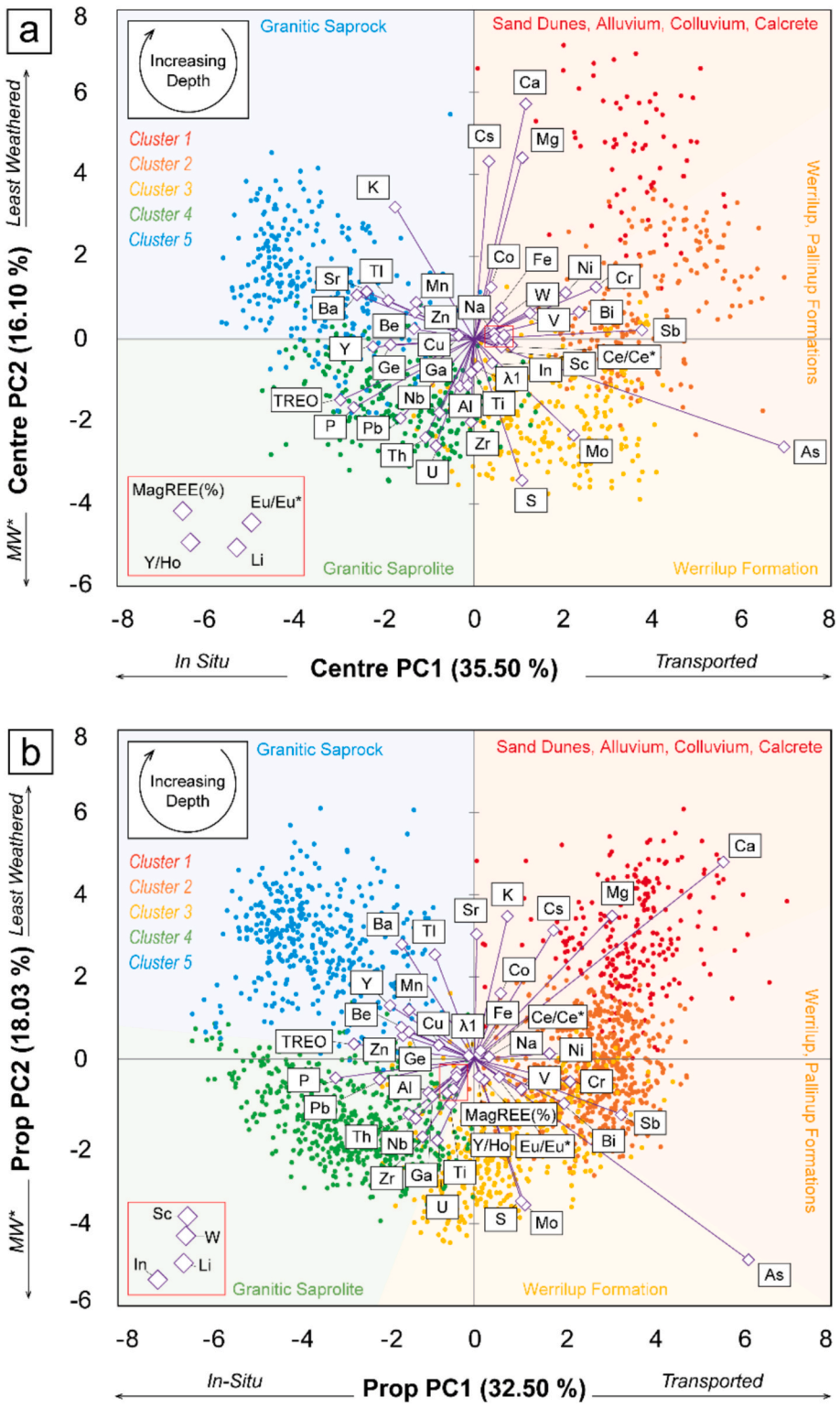

Fig. 6. Principal component analysis (PCA) of regolith samples from the Centre prospect (a) and the Prop prospect (b), grouped into their five clusters derived from K-means analysis. The primary axis of variation across both prospects appears to be anticorrelations between the lithophiles (in situ) and chalcophiles/siderophiles (transported) across PC1, as well as anticorrelations between the fluid mobile elements (whose high concentrations represent the 'least weathered' rocks) and fluid-immobile elements (representing the 'most-weathered' rocks) across PC2. These associations neatly characterise all five clusters in a clockwise direction with increasing depth and are applied in the remainder of the text to define element ratios for cluster discrimination.

geochemically characterisable by the PCA, which offered no indication that the analyses had been affected by outlier values (Filzmoser et al., 2009). Various trends were consistent between each prospect. Across both, the five clusters positioned themselves such that their increase in depth (Figs. 4 and 5) corresponded with clockwise rotation around the PCA diagram (Fig. 6). This positioning aligned with a loose separation of Goldschmidt element classifications across the four quadrants, as constrained by positive and negative values of Principal Component 1 (PC1)

and Principal Component 2 (PC2). Generally, the negative values of PC1 encompassed the lithophile elements (K, Be, Y, P, U, Ti, Th, Nb, Zr, Al, Hf and the REEs), whereas positive values of PC1 encompassed the siderophile elements (Fe, Co, Ni, Mo and W) and chalcophile elements (S, As, In, Bi and Sb). The largest Ce anomalies (Ce/Ce*), the largest Eu anomalies (Eu/Eu*) and the largest MagREE percentages (MagREE%) also align along positive values of PC1. Conversely, the most positive values of PC2 are largely (though not entirely) reserved for the elements that may be considered the 'most-fluid-mobile' (Ca, Mg, K, Cs, Tl, Ba, Sr, Middelburg et al., 1988), whereas the 'least-fluid-mobile' elements (i.e., the high field strength elements [Zr, Ti and Nb], Th, Al, Y and the REEs), as well as λ1 occupy negative values across PC2. Interpretations as to the geological controls on PC1 and PC2 are preliminarily included in Fig. 6 but are properly addressed further in the discussion. The factor loadings for PCA are given in Table 2. Other summary PCA statistics can be found in the ESM.

4.3. Hyperspectral mineralogy and element ratios

To facilitate the validation and characterisation of the above k-means clusters in a geological context, they are referenced against two hyperspectral logs collected from drill cores in the Centre prospect (Fig. 7). The results of these mineralogical analyses are reported in this section, alongside variations in element ratios, concentrations and indices throughout the same drill cores and between the clusters. Abbreviations and descriptions of these ratios, as well as how they were calculated, can be found in Table 1, whereas the exact reasons for these ratios being chosen can be found in the discussion. Clusters are characterised in reverse order (5-1) from the deepest (often youngest) chemostratigraphic horizons (Clusters 5 and 4) to the shallowest regolith horizons (Cluster 1, Fig. 4). Average values for each of the geochemical descriptors outlined below are also given in Table 3. The fundamental generalisations made in the following paragraphs are based on this set of average values.

4.3.1. Cluster 5

Cluster 5 has low abundances of quartz, plagioclase, and K-feldspar, relative to high contributions of moderately crystalline kaolinite (Fig. 7). It contains negligible contributions of Fe-oxides or smectite and is broadly light-to-dark grey in colour. Cluster 5 has the highest average TREO abundances and MagREE percentages of any cluster (Table 3) and moderately high λ1 values that are exceeded only by Cluster 4. Its Y/Ho ratios are among the highest (alongside Cluster 1) and it exhibits neutral to slightly negative Ce anomalies. Its Al/K ratios and transported metal index (TMI) values are the lowest. Its weathering enrichment index (WEI) is second highest to Cluster 1, while its chemical index of alteration (CIA) is second lowest (again to Cluster 1). It also exhibits the lowest Sb/Y ratios and high Cs/Th ratios.

Table 2
Principal component analysis factor loadings from the Centre and Prop datasets.

Variable	Centre					Prop				
	F1	F2	F3	F4	F5	F1	F2	F3	F4	F5
Al	−0.04	−0.19	−0.08	−0.17	−0.12	−0.23	0.14	−0.10	−0.09	−0.07
As	1.78	−0.45	0.38	0.35	0.22	1.44	0.85	0.18	0.20	0.07
Ba	−0.67	0.18	0.16	−0.01	0.47	−0.38	−0.49	−0.12	0.25	0.13
Be	−0.34	0.04	−0.10	0.06	−0.09	−0.38	−0.14	−0.02	−0.10	0.06
Bi	0.60	0.11	−0.18	−0.24	0.03	0.47	0.19	−0.21	−0.06	0.17
Ca	0.30	0.99	−0.18	0.80	−0.47	1.31	−0.84	0.73	−0.50	−0.16
Co	0.10	0.22	0.09	0.43	0.10	0.14	−0.28	−0.07	−0.02	0.22
Cr	0.70	0.22	−0.18	−0.17	0.21	0.51	0.10	−0.37	−0.11	0.26
Cs	0.09	0.75	0.40	−0.41	0.06	0.42	−0.55	−0.37	0.43	−0.07
Cu	−0.09	0.01	−0.16	0.02	0.08	−0.19	−0.06	−0.07	−0.19	0.17
Fe	0.16	0.13	−0.22	−0.02	0.06	0.03	0.07	−0.19	−0.13	0.13
Ga	−0.08	−0.20	−0.13	−0.20	−0.12	−0.23	0.15	−0.16	−0.11	−0.07
Ge	−0.48	−0.02	−0.04	0.10	0.01	−0.34	−0.12	0.13	0.02	0.03
In	0.10	−0.10	−0.15	0.01	0.09	−0.14	0.14	−0.03	−0.09	0.14
K	−0.45	0.55	0.63	−0.36	0.02	0.18	−0.61	−0.28	0.51	−0.18
Li	0.16	0.00	−0.22	−0.04	−0.16	−0.11	0.13	0.14	−0.17	−0.06
Mg	0.27	0.76	−0.08	−0.06	0.05	0.73	−0.61	−0.01	0.02	0.07
Mn	−0.33	0.15	−0.21	0.22	−0.10	−0.34	−0.21	0.12	−0.23	0.01
Mo	0.57	−0.40	0.12	0.04	0.06	0.27	0.62	0.11	0.19	−0.12
Na	0.11	0.06	0.06	−0.16	−0.01	0.13	0.08	−0.07	0.11	0.02
Nb	−0.20	−0.31	−0.20	−0.05	0.05	−0.31	0.25	−0.04	−0.07	0.04
Ni	0.52	0.19	−0.03	0.30	0.18	0.37	−0.02	−0.14	−0.05	0.32
P	−0.69	−0.29	−0.20	0.23	0.30	−0.73	0.08	0.32	0.10	0.36
Pb	−0.42	−0.33	0.06	0.02	−0.10	−0.50	0.09	0.13	0.00	−0.09
S	0.27	−0.59	0.70	0.36	−0.14	0.25	0.61	0.59	0.59	0.06
Sb	0.96	0.04	−0.03	−0.08	0.09	0.77	0.24	−0.12	−0.04	−0.09
Sc	0.16	−0.03	−0.22	−0.08	0.07	−0.09	0.07	−0.17	−0.16	0.21
Sr	−0.62	0.20	0.03	0.29	0.38	0.01	−0.53	0.46	0.11	0.24
Th	−0.28	−0.41	−0.01	−0.01	−0.23	−0.34	0.24	0.09	−0.06	−0.29
Ti	−0.02	−0.14	−0.27	−0.08	0.15	−0.12	0.19	−0.10	−0.09	0.12
Tl	−0.49	0.16	0.65	0.02	0.00	−0.21	−0.44	−0.11	0.43	−0.20
U	−0.22	−0.45	0.08	0.08	−0.06	−0.19	0.35	0.26	0.11	−0.13
V	0.32	0.11	−0.30	−0.06	0.28	0.25	0.13	−0.21	−0.11	0.30
W	0.14	0.09	0.07	−0.20	−0.28	−0.03	−0.01	−0.23	−0.05	−0.29
Y	−0.58	−0.03	0.01	0.16	0.02	−0.44	−0.23	0.28	−0.01	0.09
Zn	−0.34	0.11	−0.02	0.15	0.00	−0.37	−0.10	0.14	0.05	0.07
Zr	−0.02	−0.35	−0.05	−0.13	−0.11	−0.27	0.33	−0.02	−0.09	−0.29
TREO	−0.77	−0.25	−0.05	0.21	−0.05	−0.63	−0.06	0.39	0.02	0.02
MagREE (%)	0.11	0.02	−0.01	−0.15	−0.11	0.03	−0.04	−0.08	−0.11	−0.15
Y/Ho	0.12	0.01	−0.02	−0.14	−0.17	0.03	−0.02	−0.07	−0.16	−0.21
λ1	0.02	−0.11	−0.04	−0.11	−0.18	−0.09	0.06	0.02	−0.13	−0.20
*Ce/Ce**	0.21	−0.03	−0.07	−0.12	−0.23	0.05	0.09	−0.10	−0.21	−0.24
*Eu/Eu**	0.17	0.02	−0.03	−0.16	−0.13	0.08	−0.01	−0.12	−0.13	−0.14

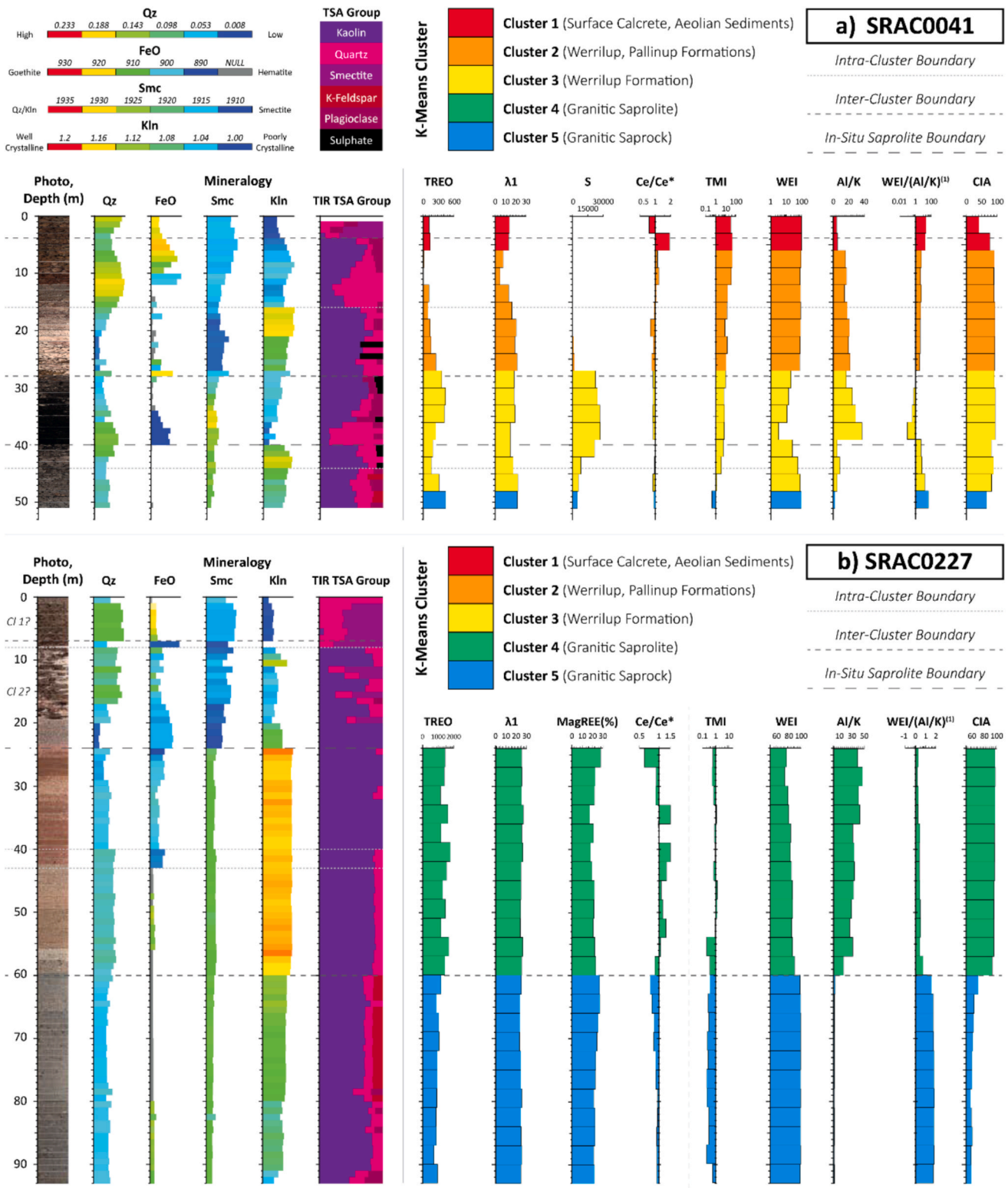

Fig. 7. Representative drill core logs from the Centre prospect, in which hyperspectral mineralogy is aligned to the clusters defined by K-means analysis and various element ratios that are discussed throughout this paper. Granitic saprolites and saprocks formed in situ at Splinter Rock are generally characterisable by their low abundances of smectite, their high abundances of kaolinite, their high TREO values and their low TMI values (TMI < 1) relative to the transported sediments (Werrilup and Pallinup Formations) as represented by Clusters 1–3.

4.3.2. *Cluster 4*

Cluster 4 sits above Cluster 5 and is accompanied by sharp variations in mineralogy and geochemistry. Cluster 4 contains no amounts of plagioclase, K-feldspar or smectite and is dominated by highly crystalline kaolinite and small percentages of quartz. Quartz contents notably influence the colour of the Cluster 4 horizon, changing it from grey (higher percentages of quartz, Fig. 7a) to light brown and eventually red/pink (lower percentages of quartz, Fig. 7b). Colour differences

Table 3
Average concentrations and values of select elements and element ratios from the Centre prospect (n = 1087) and the Prop prospect (n = 2185), divided into clusters that represent the in situ weathered granites (Clusters 4 and 5) or their overlying transported sedimentary materials (Clusters 1, 2 and 3).

Prospect		Centre					Prop				
		Transported			In Situ		Transported			In Situ	
Cluster		*1*	*2*	*3*	*4*	*5*	*1*	*2*	*3*	*4*	*5*
Element Concentrations (ppm)	*Al*	54345	74606	93133	107146	84349	47015	62677	82363	100538	84380
	Fe	29186	32203	29071	31141	34132	23984	34412	31943	32182	32600
	Ca	66761	720	1922	673	1905	82035	3223	3705	584.6	1287
	Mg	15613	3106	1206	938.5	3226	23776	5744	4031	988.4	5175
	Na	4552	6007	4303	3537	6056	6284	8982	10710	5184	6949
	K	9204	8401	7084	3787	44993	13601	14055	10479	3695	34802
	P	105.2	160.3	383.3	831.3	1160.4	123.4	98.17	322.9	452.5	772.4
	S	1210	2396	14349	1513	1464	1909	1408	15486	1386	1097
	Th	30.50	44.11	106.33	150.41	120.49	19.69	22.69	47.96	58.96	48.83
	U	2.71	4.08	12.45	12.97	10.15	2.05	1.79	8.72	3.93	2.88
REE Concentrations and Ratios	*TREO*	398.97	186.95	569.70	1264.12	1342.63	230.60	127.12	389.13	489.20	648.18
	MagREE (%)	24.42	22.74	22.82	20.68	25.22	25.48	22.75	22.96	21.93	25.79
	λ1	17.20	18.05	21.33	24.98	23.47	17.03	16.34	20.55	21.59	20.83
	*Ce/Ce**	1.06	0.97	0.96	1.26	0.84	1.04	1.11	1.09	1.35	0.95
	*Eu/Eu**	0.62	0.55	0.54	0.53	0.58	0.64	0.63	0.58	0.60	0.64
	Y_ppm	28.33	11.75	27.97	39.04	65.13	23.39	8.15	21.96	24.10	44.11
	Ho_ppm	1.02	0.47	1.08	1.48	2.33	0.83	0.34	0.89	0.97	1.60
	Y/Ho	28.00	25.07	25.73	26.31	28.39	28.06	24.46	24.40	24.79	27.00
Other Indices and Element Ratios	*WEI*	96.77	81.43	43.36	71.34	96.15	97.38	91.53	48.99	73.19	95.73
	TMI	19.32	15.55	6.78	1.82	0.51	15.56	20.75	11.15	6.94	1.82
	CIA	48.66	82.48	87.22	92.59	62.94	34.8	69.59	77.46	91.27	66.78
	Al/K	7.02	9.91	23.77	34.91	2.09	3.78	5.59	13.71	43.04	3.75
	Cs/Th	1.0644	0.0332	0.0057	0.0017	0.0210	0.1009	0.0981	0.0284	0.0086	0.1080
	Sb/Y	0.0543	0.1293	0.0195	0.0041	0.0020	0.0354	0.1213	0.0293	0.0127	0.0041

may also be influenced by the relative percentages of FeO, which are notably higher in the brown/pink examples of Cluster 4 than they are in the grey examples. Cluster 4 exhibits high TREO concentrations (exceeded only by Cluster 5) and the highest λ1 values. Cluster 4 contains variable Ce anomalies depending on depth (Figs. 4, 5, 7b), though they are the largest (Ce/Ce* = 1.26 and 1.35 in Centre and Prop) on average. Cluster 4 has the lowest MagREE percentages, the highest Al/K ratios and exhibits low-to-moderate TMI values. It has moderate WEI values, the highest CIA values, and the lowest Cs/Th ratios.

4.3.3. Cluster 3

The kaolinite-dominated layers of Cluster 4 are superseded by a quartz- and Fe-oxide-rich horizon at the base of Cluster 3, which gradually grades upwards through a plagioclase-bearing unit and finally a kaolinite-rich unit at the top of the cluster (Fig. 7a). Kaolinite crystallinity gradually decreases with depth throughout Cluster 3, which is characteristically smectite-poor. Unlike in Clusters 4 and 5, sulphate minerals are also detected towards the top of Cluster 3, in correspondence with: 1) significant increases in S concentrations, and; 2) a colour shift to one that is often (but not always) black (Fig. 7a). Compared to Cluster 4, Cluster 3 exhibits lower TREO concentrations, lower λ1 values and higher MagREE percentages. Ce anomalies in Cluster 3 are neutral-to-positive (average Ce/Ce* = 0.96 and 1.09 in Centre and Prop). Cluster 3 exhibits the lowest WEI, moderate TMI and moderate CIA values. Its Al/K ratios are second-largest, its Cs/Th ratios are second-lowest and its Sb/Y ratios are moderate.

4.3.4. Cluster 2

Relative to Cluster 3, Cluster 2 is characterised mineralogically by a sharp increase in smectite abundances and a significant increase in kaolinite crystallinity, alongside a notable increase in quartz contents relative to a decrease in plagioclase. Its TREO contents decrease notably from Cluster 3, as do its λ1 values. Cluster 2 exhibits variable Ce anomalies (average Ce/Ce* = 0.97 and 1.11 in Centre and Prop) and slightly increased Eu anomalies (average Eu/Eu* = 0.55 and 0.63 in Centre and Prop). It exhibits moderate-to-high WEI values, the second highest TMI values in Centre and the highest TMI values in Prop. Its CIA values remain relatively high, as do its Al/K ratios (Table III). Its Cs/Th values are high (second highest in Centre and third in Prop) and its Sb/Y values are the largest across all clusters.

4.3.5. Cluster 1

Cluster 1 contains notable concentrations of quartz, high concentrations of smectite, low-to-moderate concentrations of FeO and low amounts of poorly crystalline kaolinite. It exhibits an increase in TREO relative to Cluster 2, as well as a notable increase in MagREE percentages (Table 3). Its λ1 values are lowest at Centre, second lowest at Prop and it exhibits neutral to slightly positive Ce anomalies (Ce/Ce* = 1.06 and 1.04 in Centre and Prop). Its Y/Ho ratios are among the largest (with Cluster 5) and its WEI values are the largest. Its TMI values are highest and second highest in Centre and Prop, respectively, whereas its CIA values are notably low. It has low Al/K ratios, high Cs/Th ratios and high Sb/Y ratios.

4.4. Metallurgical test work

All percentages of REEs extracted from select samples across the Centre and Prop prospects via leach testing, as well as the values of acid consumption for each sample, are given in ESM1. Head assay TREO grades of the samples ranged between 468 ppm (SRAC0222, Clusters 2, 3) and 3315 ppm (SRAC0402, Cluster 4). Head assay MagREE grades ranged between 89 ppm (SRAC0222, Clusters 2, 3) and 1028 ppm (SRAC0271 [21–30 m], Clusters 4, 5). Recoveries of the MagREEs ranged between 10 % (SRAC0298, Clusters 3, 4) and 90 % (SRAC0217, Clusters 4, 5). Acid consumptions ranged between 11 kg/t (SRAC0432, Clusters 4, 5) and 136 kg/t (SRAC0271 [30–45 m], Cluster 5). The trends in MagREE grade, recoverable MagREEs and acid consumption in relation to various regolith horizons (i.e., k-means clusters), as well as their effect on defining REE mineralisation, are addressed in the discussion.

5. Discussion

5.1. Delineating regolith horizons via unsupervised geochemical clustering

The identification of five laterally- and chemically dependable regolith horizons at Splinter Rock via k-means clustering analysis (Figs. 4 and 5) indicates that this technique can successfully group large numbers of regolith samples into well-defined stratigraphic layers based on whole-rock geochemistry. That these clusters represent real stratigraphic layers is broadly supported by the fact that similarly shaped regolith horizons have previously been identified around the Esperance REE district (Trench et al., 2024). However, to provide confidence on how accurately these clusters define 'real' stratigraphic boundaries, it is important to corroborate these results against detailed mineralogical and geochemical analyses (such as those obtained by hyperspectral analysis, Fig. 7) and to use this information to interpret the regolith layers in a geological context. This section attempts to validate the results of k-means analysis by interpreting the geological nature of all five clusters (through their corroboration against mineralogical and geological data), before discussing the overall accuracy and limitations of k-means clustering analysis of whole-rock geochemical data as a means to define large regolith horizons.

5.1.1. Clusters 5 and 4: saprock and saprolite

Granites are subject to various mineralogical and geochemical transformations during weathering, that provide a first-order control on the formation of regolith-hosted REE deposits. Relevant mineralogical transformations include: 1) the destruction of primary aluminosilicate minerals (i.e., feldspars and micas) and their replacement by secondary aluminosilicate clays (i.e., kaolinite and halloysite) which provide negatively-charged surfaces for dissolved REE ions to absorb and accumulate (Jeong, 2000; Robertson and Eggleton, 1991; Yang et al., 2019); 2) the progressive crystallographic evolution of those clays from poorly-crystalline (defect-rich) to highly-crystalline (defect-poor) morphologies (Papoulis et al., 2004; Tsuzuki and Kawabe, 1983), which results in reduced surface areas and REE desorption (Bamforth et al., 2024b; Yang et al., 2019), and; 3) the dissolution of primary phosphate-bearing minerals (i.e., apatite, monazite), prior to that dissolved phosphate reacting with dissolved REEs to precipitate insoluble secondary minerals like rhabdophane ($REEPO_4{\cdot}xH_2O$, $x = 0$–1), monazite ($REEPO_4$) and florencite ($REEAl_3(PO_4)_2(OH)_6$) (Bamforth et al., 2024b; Sanematsu et al., 2015). Some common and relevant geochemical features of granite weathering include: 1) downwards mobilisation of the REEs through the weathering profile, prior to accumulation at lower stratigraphic positions (Bao and Zhao, 2008; Li et al., 2017; Sanematsu and Watanabe, 2016); 2) the formation of positive and negative Ce anomalies at the tops and bottoms of weathering profiles, respectively (Braun et al., 1990; Ichimura et al., 2020; Kalintsev et al., 2021), and; 3) highly variable vertical fractionation of the LREEs and HREEs (Li et al., 2017), due to greater HREE-complex stabilisation and mobilisation over a broader range of pH conditions and stratigraphic positions (Liu et al., 2022; Nesbitt, 1979; Yusoff et al., 2013).

These mineralogical and geochemical features are observed across Clusters 5 and 4 at Splinter Rock. Both clusters are dominated by kaolinite, quartz and small percentages of remnant K-feldspar and plagioclase (in Cluster 5) that are gradually replaced by kaolinite in Cluster 4. The crystallinity of this kaolinite also increases systematically towards higher stratigraphic positions (i.e., Cluster 4), as is consistent with gradually intensified weathering. Such mineralogical features indicate a lithophile-rich composition, which is supported geochemically by the low TMI values and PCA analysis of both clusters (Fig. 6). Rare earth element concentrations and $\lambda 1$ values in Clusters 5 and 4 decrease with depth, as is consistent with downwards REE mobilisation and a decrease in LREE/HREE ratios, respectively. There are clear zones of oxidative weathering that are characterised by a transition from positive Ce anomalies to negative Ce anomalies at the interface between Clusters 4 and 5, such as within drill holes (SRAC)0217–0220 and 0226–0227 (Fig. 4c) as well as drill holes 0149, 0150, 0253 and 0254 (Fig. 5c). Indices and ratios that are designed to measure the extent of weathering (i.e., WEI, CIA, Al/K) also drop sharply at this boundary, as is diagnostic of most saprolite-saprock boundaries in altered granites (Gong et al., 2013; Liu et al., 2016; Sanematsu et al., 2013). These mineralogical and geochemical features indicate that Clusters 5 and 4 represent the saprock (i.e., Cluster 5) and its overlying saprolite that formed during chemical weathering (i.e., Cluster 4). The intense oxidative weathering that formed this saprolite is loosely interpreted to have occurred under sub-tropical conditions from the late-Permian to the late-Cretaceous (Anand and Butt, 2010); a lack of evidence for CIA variation within the overlying sediments (Fig. 7) supports previous interpretations that these were not intensely weathered (Anand and Paine, 2002; Salama and Anand, 2017), such that the weathering responsible for saprolite formation likely occurred prior to Eocene sedimentation (Fig. 2). Lastly, the assignment of Clusters 5 and 4 to a granitic source rock confirms that its saprock and saprolite host the majority of REE accumulation (Table 3), as is true for most regolith-hosted REE deposits (Li et al., 2017).

5.1.2. Clusters 3-1: transported sediments

The formation of saprolite across the Yilgarn Craton and Albany-Fraser Orogen during the late-Permian to late-Cretaceous was followed by an extended period of sedimentation throughout the Eocene (Anand and Butt, 2010). At Splinter Rock, these sediments are characterised by the Werrilup and Pallinup Formations (Fig. 2); a series of estuarine-deltaic strata that were deposited at the western edges of the Eucla Basin during two successive marine transgressions (Clarke, 1994; Gammon et al., 2000). One standout feature from these sequences is the upper lignitic horizon of the Werrilup Formation, which is recognised along the southern coast and may be present at Splinter Rock. Above Cluster 4 lies a black and clay-rich layer which is concentrated in S (Fig. 7a). These features are consistent with the presence of organic matter, which is often black and has a geochemical affiliation with S and other chalcophiles (i.e., As and Bi, Fig. 6). This affiliation results from the bioturbation of organic matter which: 1) enables reactive organic compounds to become available for sulphur reduction, and; 2) subsequently induces the formation of sedimentary pyrite (FeS) and the accumulation of chalcophiles in organic-rich horizons (Berner, 1985, 1984; Berner and Westrich, 1985).

In consideration of these features, this work broadly assigns Cluster 3 to the Werrilup Formation in an interpretation is further supported by: 1) the upward grading of sediments – from quartz-rich gravels and sandstones to kaolinite-rich clays (Fig. 7a) – that has previously been recognised for this sequence (Fig. 2), and; 2) the repeatedly concave cross-sectional morphology of Cluster 3 (Figs. 4 and 5), which indicates sedimentation in paleotopographic lows that were carved before or after saprolite formation by one or more pre-Eocene erosional processes (Anand and Butt, 2010). It then follows that the in-situ-transported boundary exists between Clusters 3 and 4/5, though it may not always be geochemically well-defined. In drill hole SRAC0041, for instance, the upper portion of the in-situ material is mineralogically well-defined by hyperspectral analysis and has certain geochemical features (such as high WEI values and very low Al/K values) that facilitate its clear classification not only as being in situ, but as being the saprock (i.e., with no saprolite, Cluster 4, at this location). Despite these clear markers, however, the saprock was mis-characterised as Cluster 3 by K-means analysis. This suggests that, while clustering is broadly useful for classifying regolith horizons over thousands of samples, the exact positions of regolith boundaries should be confirmed by mineralogical and geochemical analyses (for example, by comparing many ratios or characteristics) in unique instances.

In the case of SRAC0041, the mischaracterisation of saprock as Cluster 3 may have occurred in response to its relatively high proportions of S ± As, Bi (Figs. 6 and 7a). Since Cluster 3 is known to be S-

rich, it is possible that some of this S (±As, Bi) migrated down through the regolith profile in response to the influence of weathering or groundwater fluids, before accumulating in the upper portions of the weathered granite. This is evidenced by a gradual decrease in S concentrations with depth at the top of the saprock (Fig. 7a). Sulphur is highly mobile (as sulphate) under oxidising conditions, which are evidenced in Cluster 3 by: 1) the formation of sulphates in its upper layers (Fig. 7a), and; 2) a sharp transition from positive to negative Ce anomalies roughly half-way down the cluster (i.e., Fig. 5c, drill cores SRAC0150–0153, 0253, 0258–0261). It is therefore concluded that, through weathering or groundwater action, the upper portions of the granites (Clusters 4 and 5) may have become relatively enriched in chalcophile elements that were sourced from overlying sediments. This makes SRAC0041 an example of how secondary geochemical processes should be studied alongside primary mineralogical influences when defining stratigraphic horizons via unsupervised geochemical analysis.

Above the lignites of the Werrilup Formation, at least two distinct mineralogical zones are identifiable in Cluster 2 (Fig. 7a). The basal unit is lightly coloured, smectite-kaolinite rich and quartz-Fe-oxide depleted with relative mineralogical conformity, whereas the upper unit is darkly coloured, smectite-kaolinite depleted and quartz-Fe-oxide rich with evidence of upwards grading from quartz to kaolinite. While the grading features of this upper unit reflect what might be expected from the Pallinup Formation – which stratigraphically overlays the Werrilup Formation (Fig. 2) – it is more difficult to assign the lower layer to any known regional unit. Its beige colouration, clay-rich composition and mineralogical conformity with depth might indicate that it is either the Wilson Bluff Limestone formation or its spatial equivalents across the Eucla Basin, though there is not enough evidence to conclude this or that it is not still part of the Werrilup Formation. For these reasons, Cluster 2 is tentatively assigned to both the upper Werrilup and Pallinup Formations, but with distinct geochemical differences to the bulk Werrilup Formation (i.e., Cluster 3). These mainly manifest as Cluster 2 having a greater affinity for Fe-oxide-associated elements (i.e., Fe, Cr, V, Co and Ni), in addition to the chalcophile-rich compositions of Cluster 3 (i.e., high As, Bi and Sb ± S) and in agreement with the high proportions of Fe-oxides in its upper units (Figs. 6 and 7a). The associations of Cr, V, Co and Ni with these Fe-oxides requires more detailed characterisation, though they might relate to processes of redox coupling, structural incorporation or adsorption as observed in other regolith profiles (Fandeur et al., 2009; Richardson and King, 2018; Schwertmann and Pfab, 1996; Ugwu and Sherman, 2019).

Cluster 1 is a thin layer comprised of quartz and smectite-rich material (Fig. 7a) that is geochemically enriched in carbonate-associated alkali metals (K, Rb, Ca and Mg) relative to the other transported sediments. The thinness of this upper layer indicates that it probably formed more recently or by processes that do not deposit large volumes of material. Therefore, this layer was likely formed by post-Eocene alluvial, colluvial and aeolian processes and arid weathering conditions that resulted in the co-precipitation of pedogenic calcretes. Each of these surface materials has been (co)-documented in the study area (Fig. 1c, 1d, González-Álvarez et al., 2016b), though more detailed surface mapping is required to develop a better understanding of their relative distributions at Splinter Rock.

5.1.3. Summary: the usefulness of k-means clustering for defining large regolith horizons

The results discussed above demonstrate how k-means clustering can successfully define 'real' chemostratigraphic layers based only on their whole-rock geochemistry. At Splinter Rock, good overall corroboration is observed between: 1) the geochemical clusters defined by k-means analysis; 2) the variations in mineralogy and geochemistry that are defined by hyperspectral analysis, and; 3) the regolith horizons that are expected based on previous characterisation of the study area (Figs. 2 and 7).

However, it is natural that such simple approaches to characterising large regolith horizons also come with limitations. For instance, interpretation of k-means results usually leads to the identification of a small number of 'optimal' horizons which may not encompass the full geological variability present in complex regolith profiles (i.e., where the pale horizon in Cluster 2 was not independently delineated, Fig. 7). This can be addressed by increasing the 'optimal' number of clusters, though with this comes a higher risk of cluster overlap and sample mischaracterisation. Additionally, variables that strongly govern the nature of specific clusters (i.e., S in Cluster 3) may contribute to the mischaracterisation of other clusters (i.e., Cluster 4) in instances where that variable is abnormally enriched. This is observed at Splinter Rock where the upper portion of the saprolite in SRAC0041 is mischaracterised as part of the lignite horizon, possibly due to high concentrations of S in that upper portion that likely derived from the lignite and were mobilised downwards during weathering. This limitation highlights the first-order nature of k-means clustering as a method for bulk-defining approximate regolith interfaces, and the importance of applying more detailed characterisation where it is deemed essential to locate the interface exactly. Lastly, the extrapolation of cluster characteristics (defined by hyperspectral analysis) across large areas of regolith assumes a significant degree of geological and mineralogical homogeneity within those clusters – though this may not always be true. One example is the TREO grades in the saprock, which while relatively high on average at Centre (1342.63 ppm TREO, Table 2) fluctuate largely between 242.5 and 5240.4 ppm TREO across all samples. Therefore, interpreters should be aware of the likelihood for specific elements to exhibit notably variable concentrations within each of the clusters, that are not readily accounted for by the bulk k-means analysis of all elements analysed.

Regardless, as a first order means by which visually indistinct regolith samples can be rapidly defined in terms of the stratigraphic boundaries of their horizons over large samples sizes and areas, k-means analysis exhibits significant potential. This is demonstrated to be true at Splinter Rock not only for defining non-mineralised regolith horizons (i.e., Clusters 1-3) – which is necessary for identifying any ore deposit under cover – but also for defining mineralised horizons (i.e., Clusters 4 and 5) that can then be further classified in terms of their economic potential using the geochemical clusters derived.

5.2. Application to the deposit-scale characterisation of regolith-hosted REE ores

5.2.1. Identifying, defining and characterising zones of REE accumulation

As summarised above and by Li et al. (2017), most regolith-hosted REE deposits form by: 1) the destruction of weatherable REE-bearing minerals like apatite (Fu et al., 2019; Sanematsu et al., 2015; Yusoff et al., 2013), allanite (Berger et al., 2014; Ichimura et al., 2020; Sanematsu et al., 2015) and fluorocarbonates (Sanematsu et al., 2015, 2013; Santana and Botelho, 2022) – with smaller contributions from the destruction of resistate minerals like monazite, zircon and titanite (Aubert et al., 2001; Sanematsu et al., 2013) – during the chemical weathering of consolidated bedrocks that are usually granites or volcanic tuffs (Mingyuan, 1992); 2) REEs mobilisation from higher to lower stratigraphic positions (Berger et al., 2014; Fu et al., 2019; Liu et al., 2022; Santana and Botelho, 2022), which often results in fractionation between the light REEs (LREEs, La–Sm) and heavy REEs (HREEs, Eu–Lu) and relative accumulation of the latter at lower positions (Aubert et al., 2001; Bao and Zhao, 2008; Ichimura et al., 2020; Liu et al., 2022; Yusoff et al., 2013), and; 3) deposition of the REEs at these lower positions – usually around the interface between the saprolite (B-horizon) and saprock (C-horizon) – as a function of increasing fluid-rock interaction and higher pH values (Bao and Zhao, 2008; Fu et al., 2019; Ichimura et al., 2020; Sababa et al., 2021) – via secondary mineral precipitation (of minerals like rhabdophane or florencite, Bamforth et al., 2024b) or adsorption onto clay minerals (Ram et al., 2019).

Due to the low-grade and high-volume nature of most regolith-

hosted REE deposits (Jowitt et al., 2017; Li et al., 2017), mineral explorers must therefore use these trends to identify and define bulk regolith horizons that host reliably economic REE concentrations across sufficiently large volumes of material. However, while these trends corroborate well across individual studies that focus on the investigation of one or two regolith cross-sections, it is also possible for deviations to exist that can affect the bulk economic viability or extraction of REEs at the deposit scale. Depending on the regolith profile, relative LREE enrichment with depth can also occur (Condie et al., 1995), while recent work demonstrates that economic REE accumulation may also develop in transported sediments as opposed to their underlying granites (Löhr et al., 2024). The potential for these variations (especially across increasingly large areas of regolith) subsequently necessitates the detailed characterisation of regolith profiles across entire prospects. This ensures that the trends observed within localised sections (i.e., individual drill cores) are representative of the bulk deposit and can be used to develop representative ore deposit models.

If approached from a mineralogical perspective, the characterisation of thousands of regolith samples that would be required to confirm the continuity of these trends might be expected to be time-, cost- and labor-intensive. With the samples already clustered and defined via k-means analysis, however, the approach becomes rapid and intuitive. For instance, trends in TREO enrichment with depth can be plotted without cluster characterisation (Fig. 8a and b), though here no context exists as to the regolith layers that host the highest REE grades and that are likely to differ metallurgically. Conversely, by using pre-validated k-means clusters to define the regolith horizon that each datapoint belongs to (Fig. 8c and d), it is observed that the bulk of REE accumulation at Splinter Rock occurs consistently in the saprolite/saprock which makes the transported sediment-saprolite interface important to define.

This approach can also be extended to test the applicability of the literature trends described above at Splinter Rock and at the deposit scale. By taking only the data points from the well-defined saprolite (Cluster 4) and saprock (Cluster 5) horizons at both Centre and Prop, it can be observed that TREO grades generally increase down through the saprolite and towards the saprolite-saprock boundary (SSB), before decreasing away from the SSB and with increasing depth in the saprock (Fig. 9a and b). At the same time, λ1 values decrease through the saprolite towards the SSB, before increasing again through the saprock (Fig. 9c and d). These results confirm, in accordance with the literature, that TREO grades and relative HREE enrichments associated with granitic weathering at Splinter Rock are highest towards the SSB (Aubert et al., 2001; Bao and Zhao, 2008; Fu et al., 2019; Ichimura et al., 2020; Liu et al., 2022; Sababa et al., 2021; Yusoff et al., 2013), and that these

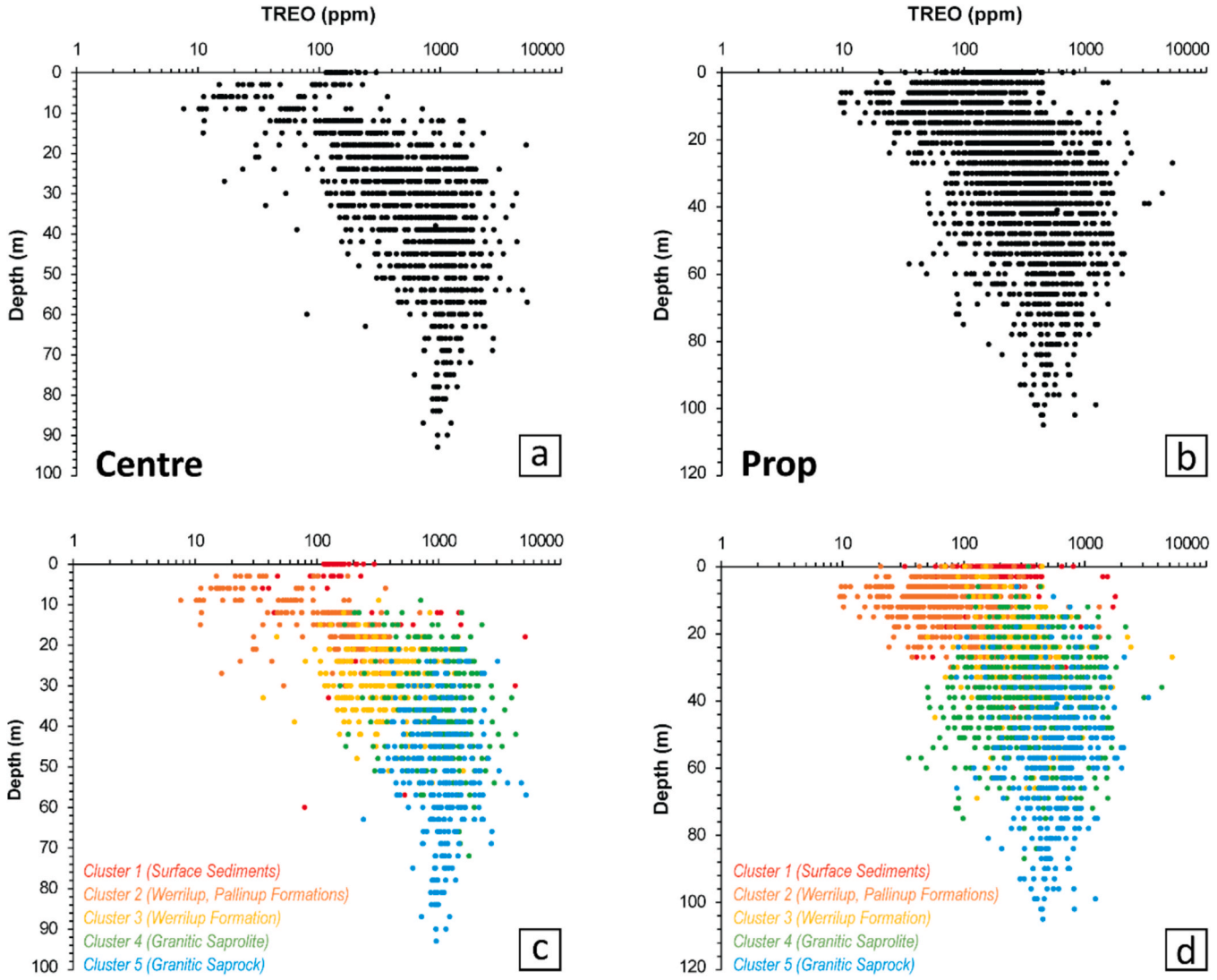

Fig. 8. Total rare earth oxide (TREO) ratios at Centre and Prop as a function of depth without (a and b) and with the integration of k-means clusters (c and d). The addition of geochemical clusters to this data highlights the granitic saprolite and saprock as, consistently, the principal host to REE accumulation at the Splinter Rock REE deposit.

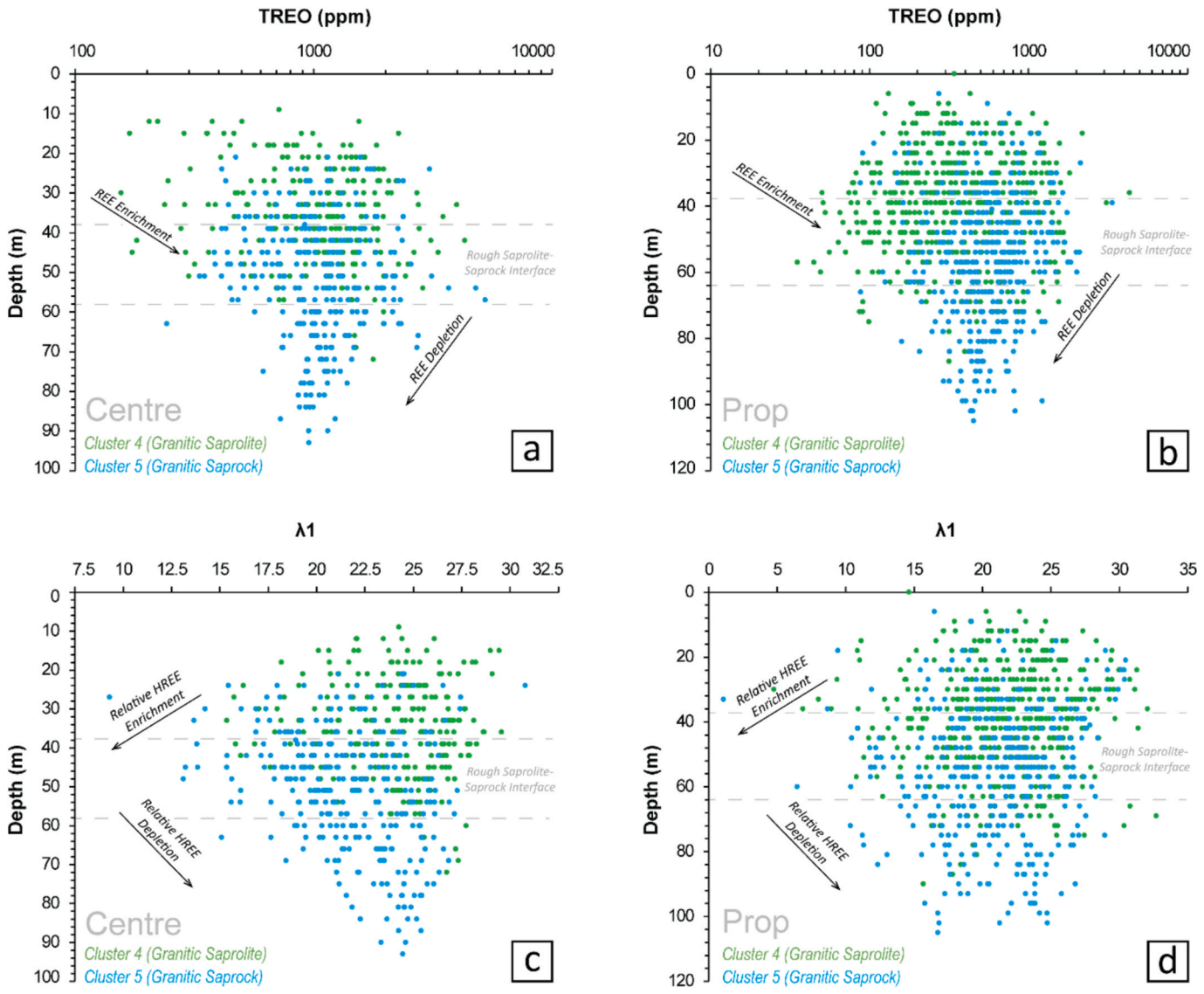

Fig. 9. Deposit scale TREO grades and λ1 values (where large numbers equal high LREE/HREE ratio) between the saprolite and the saprock at Splinter Rock. In accordance with most of the literature, the highest REE grades are found at the saprolite-saprock boundary and the HREEs become largely enriched with depth in the saprolite. Using k-means clustering, however, these trends can be rapidly validated and demonstrated at the deposit-scale.

trends are consistent at the deposit-scale rather than just representing the localised conditions of one or more well-characterised drill cores (Fig. 7). Consequently, and as with the transported-sediment-saprolite interface, the SSB becomes important to define at the deposit scale – though this is again aided by k-means clustering.

Lastly, the clusters can be used to identify and contextualise geochemical trends associated with variable Ce/Ce* anomalies in the Splinter Rock profile (Barrat et al., 2023; Braun et al., 1990; Ichimura et al., 2020). Positive Ce anomalies often form towards the tops of saprolites (and negative anomalies towards the bottom of saprolites) due to the oxidation of Ce(III) to Ce(IV), the formation of cerianite (CeO_2) or Ce(VI) incorporation into other gangue minerals, and the subsequent mired downward stratigraphic transport of Ce through the profile relative to La, Pr and Nd (Berger et al., 2014; Braun et al., 1990; Fu et al., 2019; Ichimura et al., 2020; Li et al., 2017; Zuoping and Chuanxian, 1996). In the context of economic REE accumulation, these Ce anomalies can be important to define since they may be associated with horizons that contain higher proportions of metallurgically favourable sorbed REE accumulation (Sanematsu et al., 2013, 2015) or greater TREO enrichment in general (Ram et al., 2019).

At Splinter Rock and in alignment with the literature, the deposit-scale geochemical analyses made available by k-means clustering confirm that: 1) the most positive Ce anomalies (i.e., Ce/Ce* > 1) occur almost exclusively within the saprolite, and; 2) the most negative Ce anomalies (i.e., Ce/Ce* < 1) occur largely within its underlying saprock (Fig. 10a and b). More interesting, however, is that opposite trends are observed for the relative enrichment of economically and environmentally important MagREEs; the highest MagREE percentages occur in the saprock, whereas the lowest occur in the saprolite (Fig. 10c and d). In other words, there is a strong correlation between the formation of negative Ce anomalies and relative MagREE enrichment (Fig. 10e and f) which highlights the Splinter Rock saprolite as favourable in this regard. Such a correlation makes geochemical sense, since Ce oxidation and its mired transport isolates the less valuable Ce and causes its separation from the remaining REEs during weathering (i.e., where the REEs, including Pr, Nd, Dy and Tb, are mobilised to lower stratigraphic layers without Ce to become enriched). Therefore, the oxidation of Ce in saprolite horizons can be considered a built-in and deposit-scale mechanism by which the MagREEs become enriched in supergene ores.

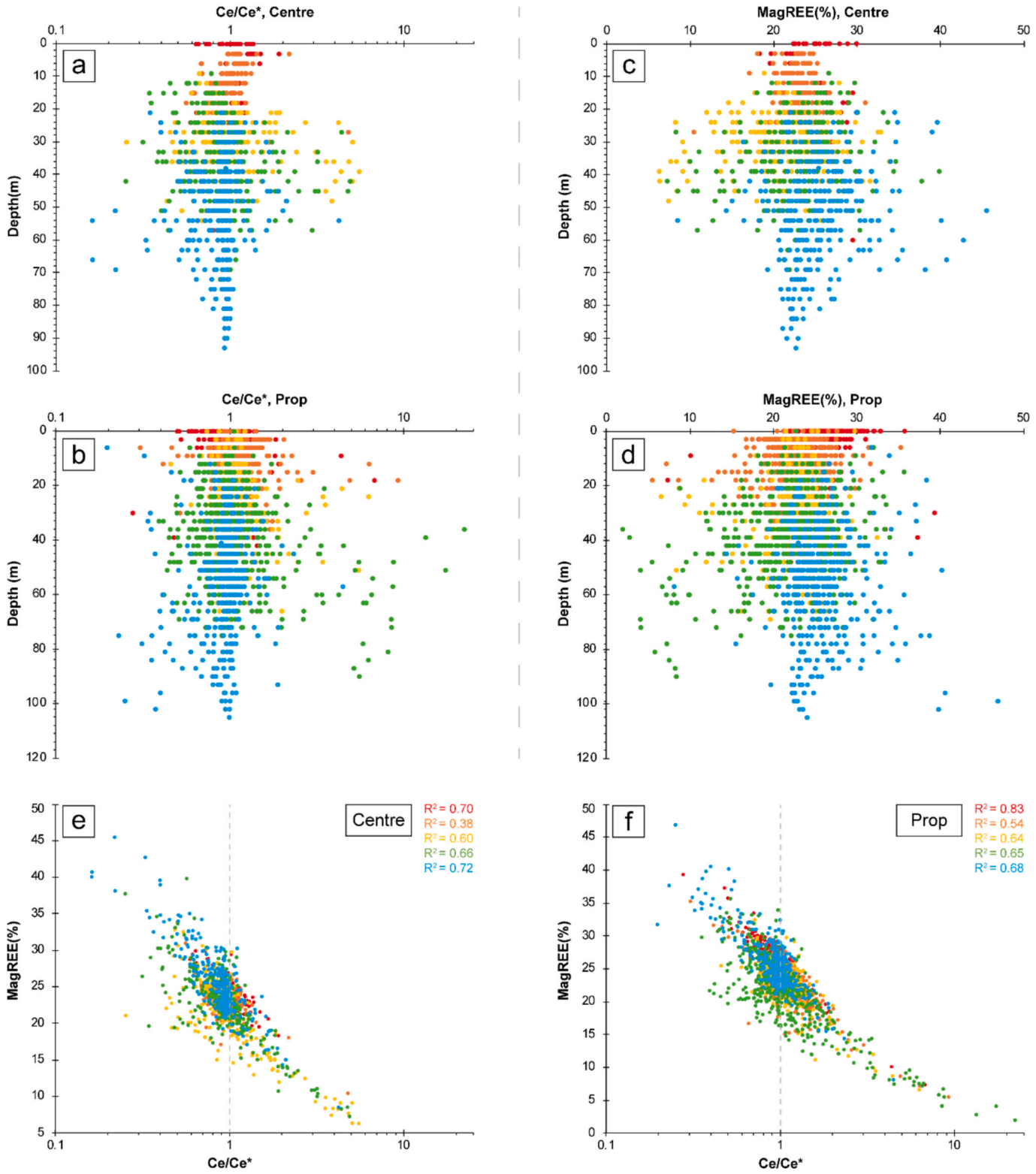

Fig. 10. Correlations between cerium anomalies (Ce/Ce*, a and b) and the relative contributions of magnet rare earth elements (MagREEs, Pr, Nd, Dy, Tb, c and d) as a percentage of all REEs at Centre and Prop. Smaller Ce/Ce* values (i.e., negative Ce anomalies where Ce/Ce* < 1) correlate strongly with higher MagREE percentages, since relative depletions in Ce within the weathering profile (that are caused by Ce oxidation and entrapment in CeO_2 at higher stratigraphic positions), aligns with relative enrichment in the remaining REEs and an increase in value (e and f).

5.2.2. Generating deposit-scale insights into REE extraction

Economic REE enrichment in regolith depends not only on these TREO grades, HREE percentages or MagREE percentages, but also on REE extractability. Specifically, economic REE extraction from regolith depends on both recovery and acid consumption, since the latter is a major capital expenditure cost. However, it is economically unfeasible for all 3000 regolith samples to be tested metallurgically. To aid in defining the most optimal zones for REE extraction across the Splinter

Rock prospect, this section assigns the k-means clusters to a small subset of samples that underwent prior metallurgical test work. The results are then extrapolated to all samples to identify possible trends across the entire prospect.

By plotting these test results in terms of MagREE grade, MagREE recovery and acid consumption, trends do emerge that indicate the metallurgical response of different regolith horizons at Splinter Rock (where some sample composites contain two clusters – with the dominant horizon being denoted by the abbreviation 'Dom' – due to test work being conducted prior to k-means analysis). Most notably, the reference samples from the saprolite horizon exhibit moderate-to-high REE grades, low REE recoveries and low acid consumption (Fig. 11a–d) whereas the selected reference samples from the saprock horizon exhibit high-to-low REE grades, high REE recoveries and high acid consumption. A degree of confidence in these interpretations is gained from the fact that both prospects independently exhibit these same patterns, such that current evidence indicates their first-order applicability to large portions of regolith via the extrapolation of these features to all cluster samples.

Overall, these results frame the SSB as being optimal from a metallurgical perspective; economic REE extraction is otherwise limited by low recoveries in the upper saprolite and higher acid consumption with increasing depth in the saprock (Fig. 11). Lower recoveries in the upper saprolite horizon may occur as a function of there being higher proportions of secondary REE minerals like rhabdophane and florencite, relative to a higher abundance of primary REE minerals like apatite, allanite and monazite in the saprock. Secondary and fine-grained REE minerals that form during weathering often precipitate in fractures and cavities associated with other minerals (Bamforth et al., 2024a, 2024b; Belogub et al., 2021; Berger et al., 2014), that may subsequently represent challenging microenvironments for the leachate to percolate. Conversely, coarse-grained primary minerals with defined grain boundaries may be more amenable to leaching, as is also suggested to be the case during the comparative weathering of adjacent granites that have variable average grain sizes (Fu et al., 2019; Santana and Botelho, 2022).

Similarly, higher acid consumption in the saprock may be expected due to greater proportions of primary Ca-Mg-K-bearing and pH-buffering minerals like silicates and carbonates in the relatively less-weathered horizon – though detailed mineralogical analysis is required to properly determine the correct controls on REE recovery and acid consumption. Irrespective of what they are, the results are consistent in that the SSB appears metallurgically-favourable across both deposits, meaning that the deposit-scale saprolite-saprock clusters and SSB defined by k-means analysis are valuable preliminary criteria for identifying and defining feasibly large zones of economic REE accumulation at Splinter Rock.

5.2.3. *Comparing the prospectivity of adjacently weathered source rocks*

Numerous studies have demonstrated how the identical weathering of adjacent sources rocks with variable compositions can lead to differences in how the REEs behave and accumulate in supergene deposits (Fu et al., 2019; Li et al., 2017; Sanematsu et al., 2015; Santana and Botelho, 2022; Yusoff et al., 2013). Differences in magma sources (i.e., S-type, A-type or I-type granites), primary P-enrichment, grain size and major element compositions contribute to determining whether a

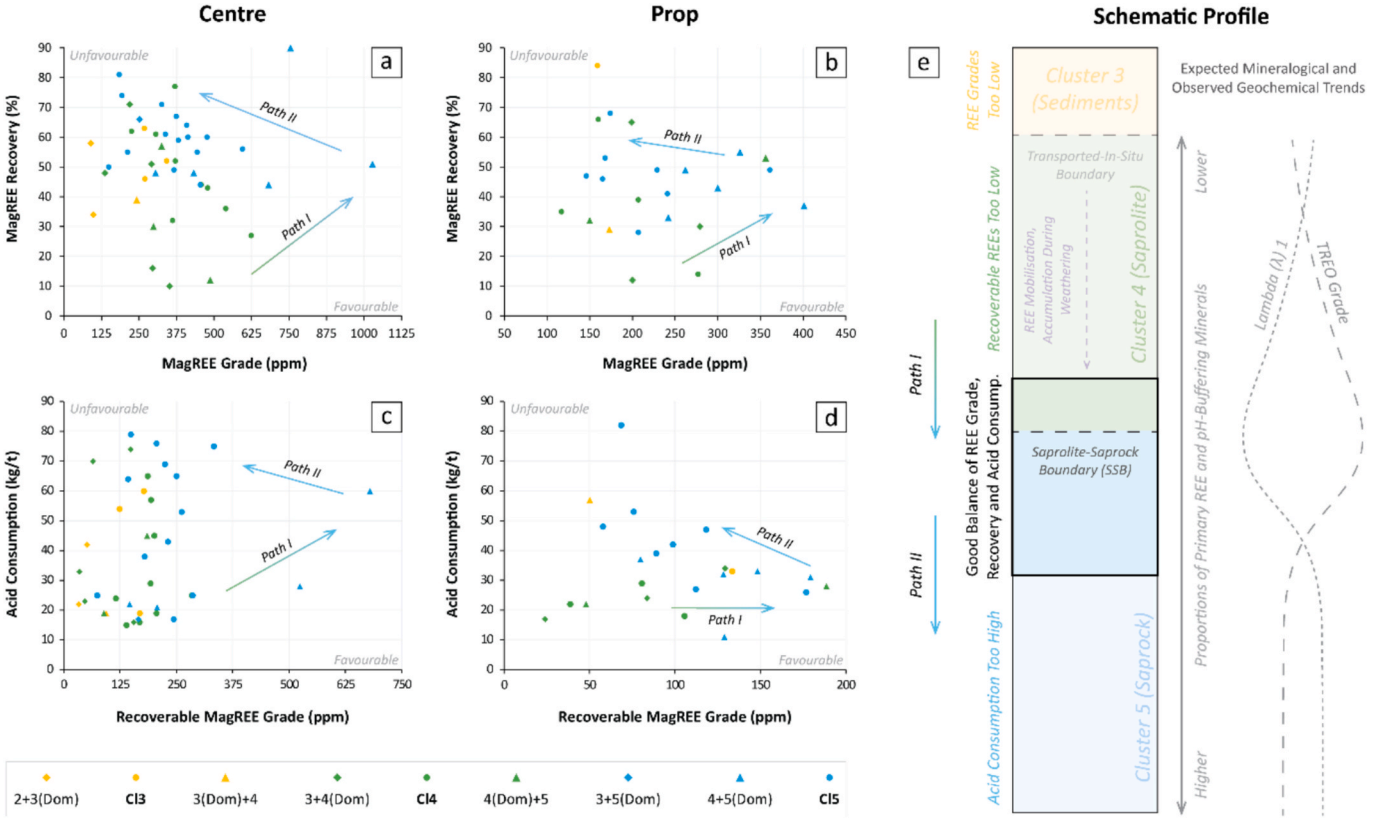

Fig. 11. Clusters derived from k-means analysis applied to the metallurgical results from the Splinter Rock prospect. Hydrochloric acid leach tests for various samples (a [Centre] and b [Prop]) found that MagREE grades were generally higher in Cluster 4 (saprolite) than in Cluster 5 (saprock), but that MagREE recoveries were higher in the latter. Composites that contained parts of both Clusters (i.e., that crossed the saprolite-saprock boundary) had the highest grade and acceptable recoveries. When recoverable MagREE concentrations (i.e., total grade * recovery) are plotted against acid consumption values (c and d), it can be seen that acid consumption is generally lower in Cluster 4 but that total recoverable MagREE concentrations are higher in Cluster 5. These results are likely a product of variable saprolite-saprock mineralogies (See Discussion) and frame the saprolite-saprock boundary as optimal for economic REE mineralisation due to its increased grade, recovery and HREE/LREE ratios.

granite will weather to accommodate regolith-hosted REE mineralisation (Li et al., 2017). However, the challenges of determining these factors in deeply weathered terrains are that: 1) a large amount of regolith material (up to 200 m in the case of Australia, Wilford et al., (2016)) may need to be drilled through to reach bedrock, which may not be uneconomical over many drill holes, and; 2) as above, the characterisation of only a few source rock samples instead may not be representative of the entire granitic intrusion.

This problem can be addressed in part at Splinter Rock through the direct comparison of materials that are interpreted to be the least weathered at Centre and Prop. Since it has been determined from PCA and the hyperspectrally-validated regolith horizons maps that Cluster 5 at both Centre and Prop is likely to represent the saprock horizon (Figs. 4 and 5), these horizons can then be compared to provide insights into the relative natures of their underlying granites. Based on the average Cluster 5 compositions at Centre and Prop (Table 3), there are likely two granites with varying compositions at each prospect. By reference to the granite at Centre, the Prop granite is notably depleted in Ca, K, and S, enriched in Mg and Na, and exhibits smaller negative Ce anomalies and λ1 values. Most significantly though, it exhibits depletions in both P and the REEs, which suggests that it's the underlying granite itself (rather than processes induced by weathering) that causes low grade REE accumulation at Prop.

It can therefore be interpreted that granitic source material (of which there could be a few, Fig. 1) at Prop is less prospective for economic REE accumulation than the one at Centre, in an interpretation that could not have been made without first defining and averaging the saprock compositions at each.

5.3. Testing and developing geochemical ratios for the classification of new samples

Depending on the stage at which the K-means analysis and PCA are conducted, it is likely that new samples will be collected and will subsequently require classification post-analysis. To prevent the need to re-do both analyses upon the addition of new samples, it may be valuable to identify one or more geochemical ratios or indices from existing samples which allow for their post-analysis classification.

5.3.1. Use of existing geochemical ratios

Ratios and indices that already exist within the literature, such as the chemical index of alteration (CIA = (Al_2O_3/[Al_2O_3 + CaO + Na_2O + K_2O]) × 100), may be fit for this purpose in some instances. For example, when the CIA (which quantifies bedrock alteration by means of quantifying the relative replacement of primary alkali-metal-rich minerals like feldspars by secondary Al-rich clay minerals like kaolinite, Nesbitt and Young, 1982) is plotted against Al/K ratios (a simpler version of the CIA that allows for variations in Ca and/or Na to be identified), the saprock and saprolite samples become definitively separable above and below values of CIA = 86 and Al/K = 11, respectively (Fig. 12). This decrease in CIA from saprolite to saprock is expected in accordance with the literature (Gall, 1994; Ichimura et al., 2020; Liu et al., 2022; Price and Velbel, 2003), and provides further confirmation of the accurate characterisation and visualisation of these horizons by k-means clustering at Splinter Rock. However, the CIA values calculated herein offer poor separation between the in-situ granitic material and the overlying transported sediments (Clusters 1–3, Fig. 12). This is likely because, as discussed above, the overlying transported sediments at Splinter Rock are unlikely to have undergone significant chemical weathering that is required for the development of highly variable CIA values with depth.

5.3.2. Development of tailored geochemical ratios

The accurate geochemical classification of new samples into one of the five k-means-defined regolith horizons at Splinter Rock will therefore require the curation of tailored geochemical ratios, which is achievable via the repurposing of PCA results. Principal component analysis excels in mapping the variables (i.e., chemical elements) that contribute most to statistical variation between all observations (whole-rock geochemical analyses). Therefore, by selecting the elements on the extremes of PC1 and PC2, one can assert that they are selecting the most optimal elements for geochemical differentiation.

Across Centre and Prop, PC1 is driven by variable concentrations of the lithophilic elements (in the granitic saprolite/saprock) and the chalcophilic/siderophilic elements (in the transported sediments) across all analyses (Fig. 6). Conversely, PC2 is driven by relative enrichments in the fluid-mobile elements (within the saprolite and surficial calcrete-hosting sand dunes) and the fluid-immobile elements that are enriched in the more highly weathered saprolite (in accordance with increased CIA values) and the basal transported sediments. The primary controls on geochemical variation in the Splinter Rock regolith are thus interpreted to be the contrasting compositions of transported and in-situ

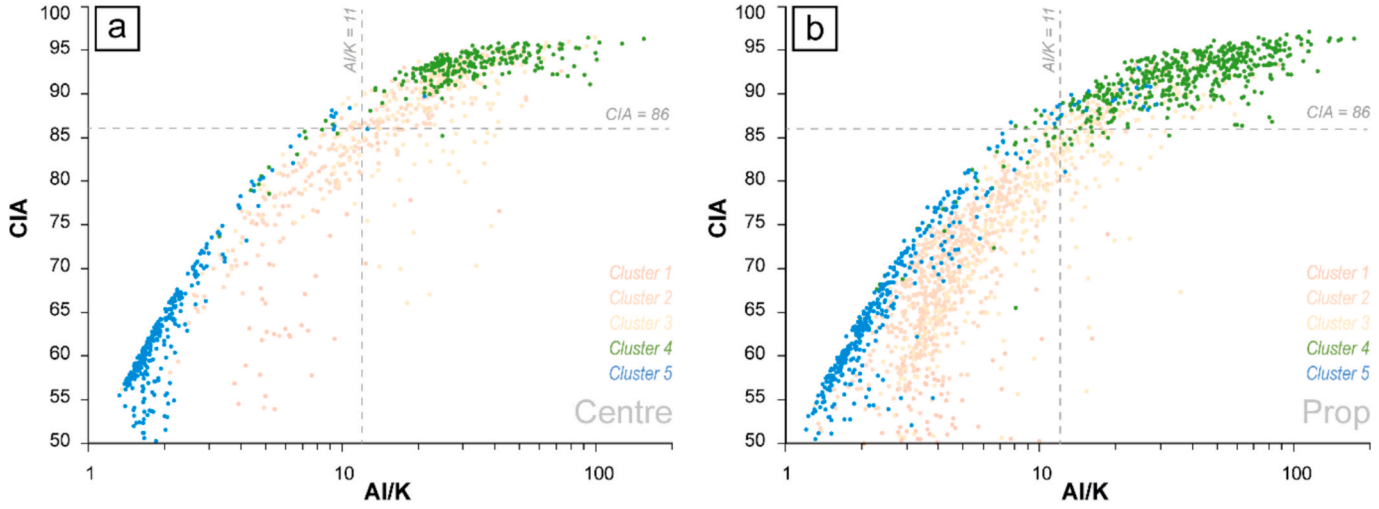

Fig. 12. Chemical Index of Alteration (CIA) values plotted against Al/K ratios for the least weathered granite (Cluster 5), its overlying saprolite (Cluster 4) and transported sediments that overly that granitic saprolite (Clusters 1–3) at Centre (a) and Prop (b). Values generate excellent separation between the saprolite and the underlying least-weathered granite (at CIA = 86 and Al/K = 11). However, the overlying transported sediments cannot be differentiated from either of these horizons by their CIA values, due to differences in their primary mineralogy and multiple weathering events that combine to cause subsequent and significant CIA value overlap.

regolith horizons (PC1) and differences in the extent of fluid-immobile element enrichment during weathering between the most highly weathered horizons (Clusters 3 and 4) and the least-weathered horizons (PC2, Clusters 1, 2 and 5). Consequently, the five clusters theoretically become separable by selecting and plotting element ratios that encompass contrasting chalcophile-lithophile concentrations (PC1) and immobile-mobile element concentrations (PC2). To best recreate the PCA results, elements that are most parallel to the x-axis (for PC1) and the y-axis (for PC2) may be selected. Here, these ratios were Sb/Y and Cs/Th, respectively (Fig. 6), which when plotted against each other recreate the fundamental PCA patterns (with successful cluster separation) using only four elements (Fig. 13).

Re-plotting the PCA results in this way allows for new samples to be assigned to their relevant regolith horizon without having to re-do the PCA or clustering analysis; the sample's Sb/Y and Cs/Th ratios can instead be added onto this plot to see with which cluster they best-align. Even so, this approach is not infallible since in some areas the clusters overlap (Fig. 13). For this reason, the ratios of new samples may also be interpreted in supplementary ways to facilitate their successful assignment. One is by mapping probable variations in these ratios with depth

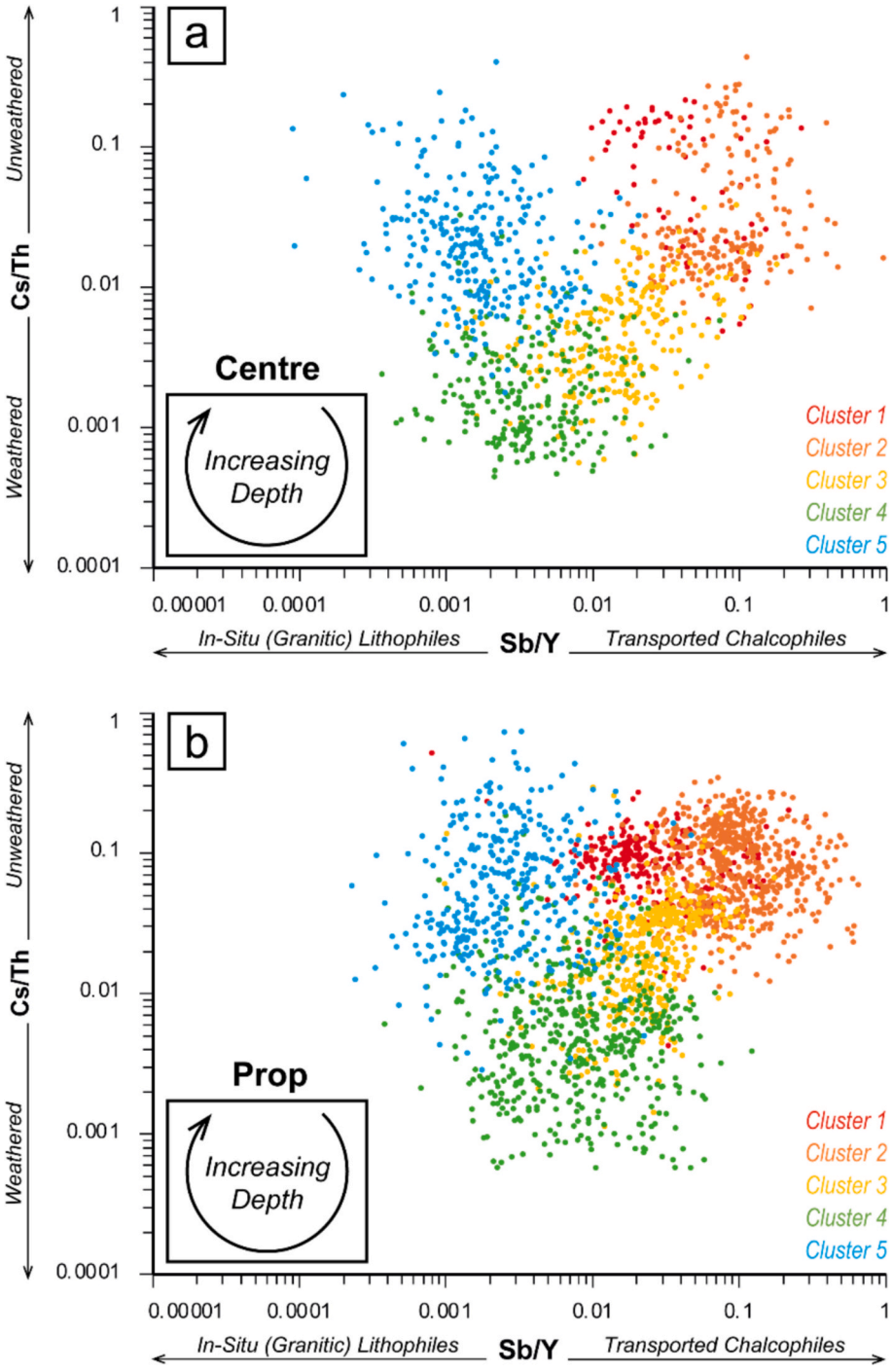

Fig. 13. Scatter plot of Sb/Y vs CS/Th for the Centre prospect (a) and Prop prospect (b). Ratios were chosen based on PCA (Fig. 6) to replicate the PCA diagram and allow for easy assignment of new assays to the current clustering scheme without re-conducting K-Means clustering and PCA. Sb/Y ratios represent the degree of transported chalcophile enrichment relative to in situ lithophile enrichment, whereas Cs/Th ratios are a proxy for weathering where lower values represent more intense chemical alteration. These ratios represent the PCA graphs with a large degree of accuracy (Centre) or with only very small rotational adjustments (Prop).

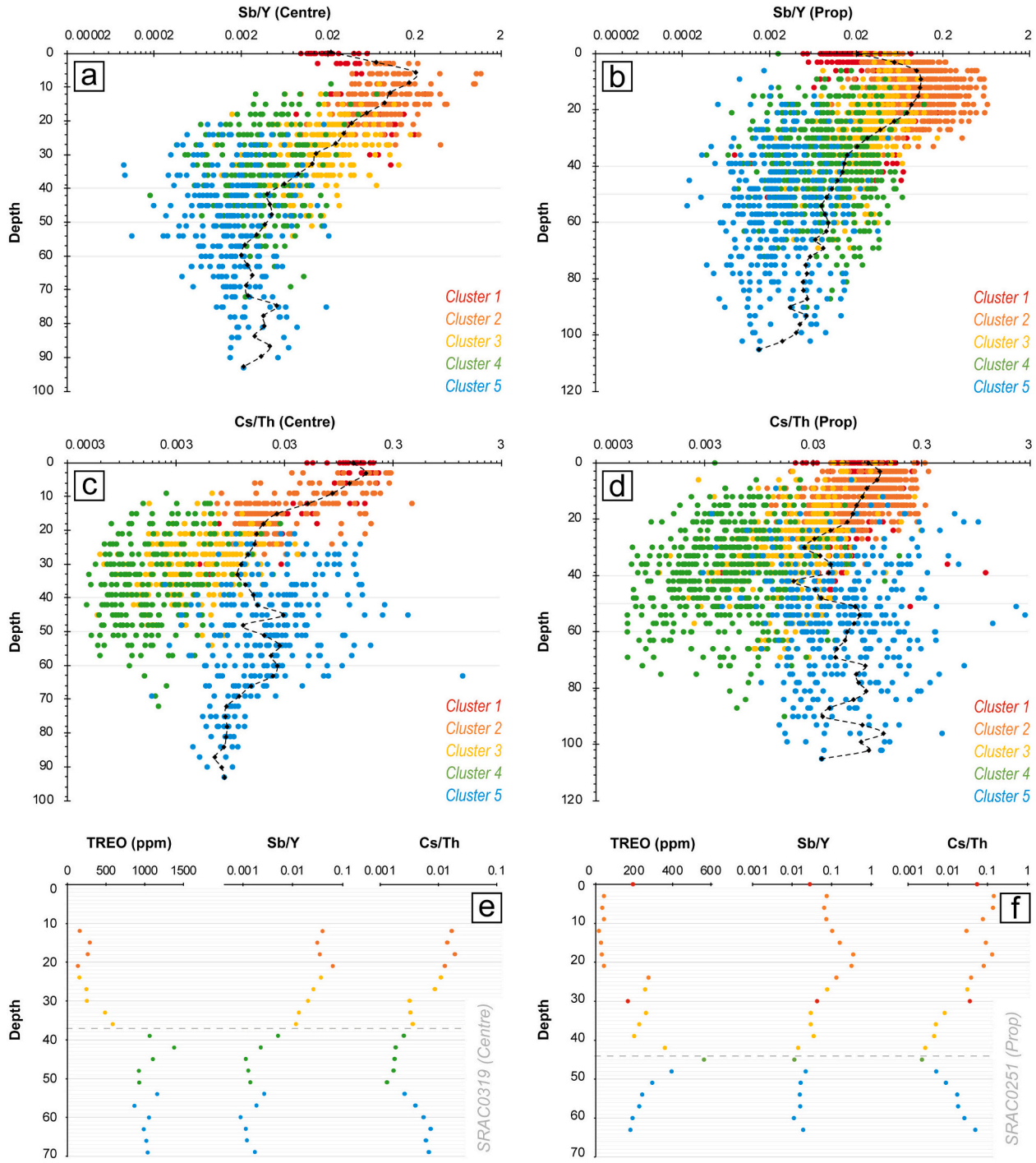

Fig. 14. All downhole values of Cs/Th and Sb/Y from the Centre and Prop prospects, showing general trends with depth (where the dashed black lines in a–d represent the average values of all samples at that depth). Cs/Th ratios are lowest in the most-weathered horizons (Clusters 2–4) and highest in the least weathered horizons (Clusters 1 and 5). Sb/Y ratios are highest in the transported sediment horizons (Clusters 1–3) and decrease systematically down to the in-situ horizons (Clusters 4 and 5). Understanding the trends of element ratios derived from PCA with assists in the accurate assignment of new assays to the correct cluster.

(Fig. 14a–d), which expectedly decrease through the profile for both Sb/Y (going from transported to in-situ horizons) and Cs/Th (going from young, less-weathered sediments to the older and highly weathered saprolite, before increasing in the saprock). These trends are observable across all samples (Fig. 14a–d) and at the scale of individual chip trays (Fig. 14e and f), such that plotting the sample depth at any scale should, alongside Fig. 12, allow for confident interpretations as to the sample's stratigraphic position and geological nature.

Lastly, further separation and confidence can be gained by developing supplementary indices whose elements independently represent each of the clusters. For example, because the eigenvectors of Cs and Th intentionally track close to the y-axis in the Splinter Rock PCA results (Fig. 6), there are a significant number of Cluster 3 and Cluster 4 data points that overlap in Fig. 13. To better separate Clusters 3 and 4 (and indeed, Clusters 1 and 5) across PC2, one element for each cluster can instead be selected for inclusion into a combined discriminatory index. Based on both prospects in Fig. 6, the elements Ca, K, S and Zr were selected for clusters 1, 5, 3 and 4, respectively, and were grouped

into their respective sides of PC2 to develop a tailored Weathering Enrichment Index (WEI, [Ca + K]/[Ca + K + S + Zr] x 100). This index subsequently represents a modified CIA that is instead: 1) based on the general mobilities of elements during weathering, rather than their specific mineralogical associations, and; 2) tailored to the Splinter Rock prospect, and the characteristic geochemical features of each of its horizons. Resultingly, when the WEI is plotted against the CIA (Fig. 15a, b), suitable separation is observed between the transported and in-situ horizons (unlike in Fig. 12) despite both representing the same process (enrichment as a function of relative element mobilities during weathering). This is especially true for the now-better separation between Clusters 3 and 4 as a result of including S within the index, which helps to better define the transported sediment-in-situ interface.

Similarly, a second index can be developed to separate all five clusters across PC1. The Transported Metal Index (TMI = [As + Cr]/[As + Cr + P + Ba] x 100) includes Cr for Clusters 1 and 2, As for Cluster 3, P for Cluster 4 and Ba for Cluster 5. Subsequently, when plotted against either the CIA or WEI, this index demonstrates good separation of the transported horizons (Clusters 1, 2 and 3) and in-situ horizons (Clusters 4 and 5) on the x-axis – as well as *between* each of the transported horizons and in-situ horizons on the y-axis (Fig. 15c–f) which can help aid in the accurate assignment of new samples.

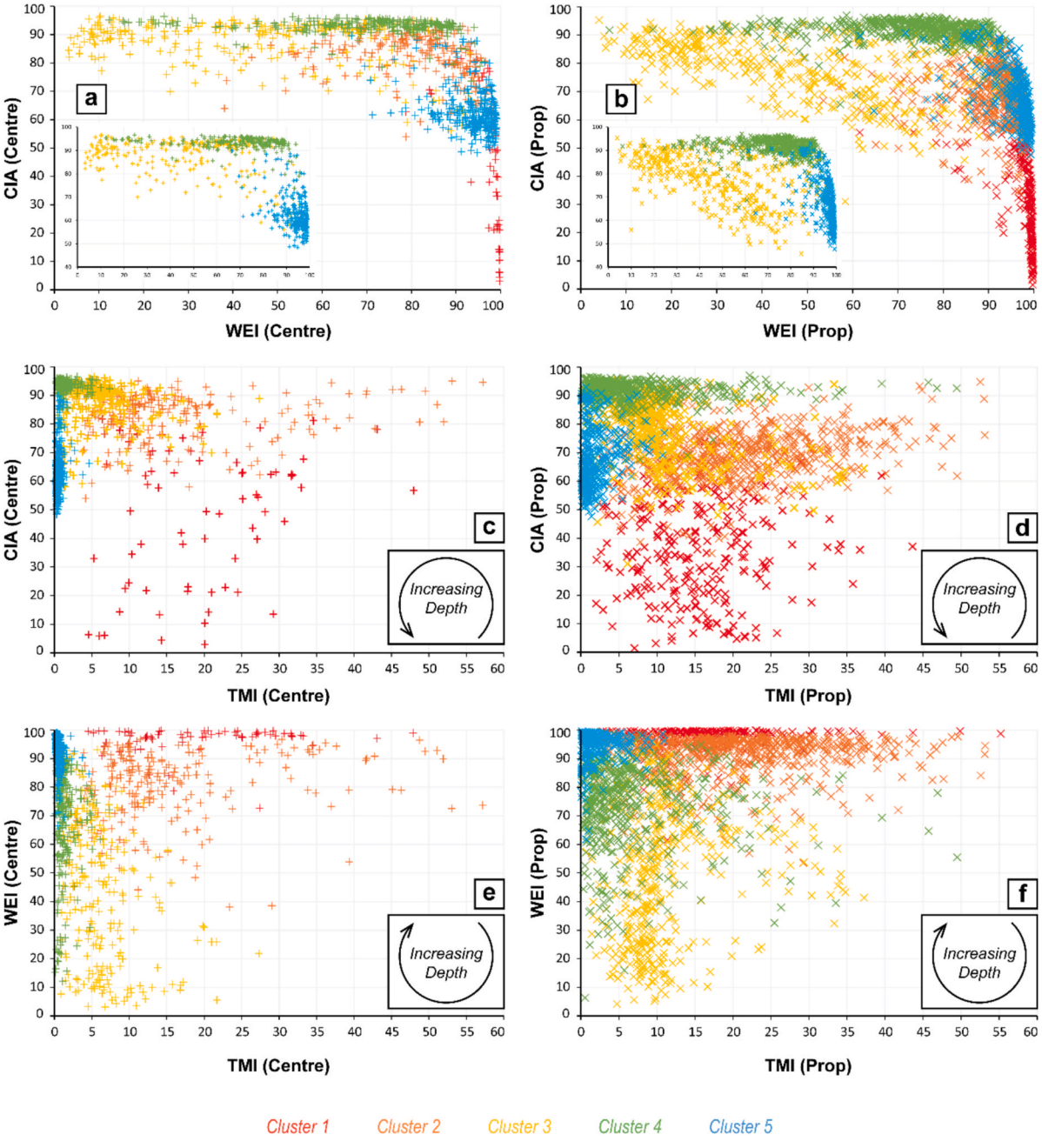

Fig. 15. Scatter plots of CIA values vs the Weathering Enrichment Index (WEI = [Ca + K]/[Ca + K + S + Zr]*100) in (a) and (b), CIA vs the Transported Metal Index (TMI = [As + Cr]/[As + Cr + P + Ba]*100) in (c) and (d) and WEI vs TMI in (e) and (f), where the left and right columns represent the Centre and Prop prospects, respectively. CIA and WEI values exhibit good correlation (as in Fig. 11), aside from Cluster 2 and especially Cluster 3 due to their high S components which drive low WEI values and separation from Cluster 4 at CIA > 80. Inset highlights this separation of Clusters 3–4 without Clusters 1 and 2. Transported sediments exhibit good separation from the in situ granitic horizons via their TMI values, especially in Prop. TMI values can be plotted against either CIA values or WEI values to cover PC1 and PC2, which facilitates the geochemical separation of clusters in various complementary ways.

6. Conclusions

Unsupervised k-means clustering succeeded in defining five geochemically distinct, laterally consistent and mineralogically validated regolith horizons at the regolith-hosted Splinter Rock REE prospect, Western Australia. In doing so, it also delineated the approximate boundaries between these horizons over hundreds of metres, thereby characterising the transported-in-situ interface and providing information as to the bulk locations and volumes of each horizon (Figs. 4 and 5). These results highlight k-means clustering as a rapid and cost-effective method through which visually indistinct regolith samples and horizons (for which sufficient geochemical analyses are available) can be preliminarily grouped and defined at the deposit-scale, thereby allowing for the bulk classification of regolith materials that may exert variable influences on geochemical and geophysical exploration below cover.

In addition to the delineation of unmineralised horizons at Splinter Rock, the broad separation of its mineralised saprolite and saprock horizons by k-means clustering allowed for the determination of important mineralisation trends at the deposit scale. As opposed to just one or two well-characterised drill cores, it was confirmed across all samples that: 1) the saprolite-saprock boundary is optimal for economic REE enrichment, due to it exhibiting the highest TREO grades, the highest HREE/LREE ratios and the most favourable metallurgical features; 2) positive and negative Ce/Ce* anomalies occur largely within the saprolite and saprock, respectively, where the latter drives increased relative abundances of the environmentally-important MagREEs, and; 3) the basement rock at Centre is more prospective than the one at Prop. The confirmation of such important trends at the deposit scale is expected to provide confidence to mineral exploration companies, which must define sufficiently large zones of mineralisation to ensure the broader economic viability of their regolith-hosted REE deposits.

Lastly, PCA was re-purposed to curate geochemical discriminators that can be used to assign new regolith samples at Splinter Rock to their appropriate horizons. It is possible that these discriminators will also find similar application at other regolith-hosted REE deposits (and especially those buried by transported sediments), since they fundamentally define both the extent of weathering and the extent of chalcophile versus lithophile enrichment which is broadly greater in transported regolith horizons. Still, these discriminators will nonetheless require further validation prior to their use within other regolith-hosted REE deposits, given the unique geochemical nature of the granites and sediments at Splinter Rock as well as the unconstrained effect of grain size on their values (Zhou et al., 2015). At the very least, the WEI and TMI represent good examples of how PCA can be used to develop tailored ratios for regolith sample assignment, which emphasises the cost-, labour- and time- effectiveness of unsupervised analyses by preventing them from needing to be rerun when introducing new samples.

CRediT authorship contribution statement

Tobias G. Bamforth: Conceptualization, Investigation, Formal analysis, Writing – original draft, Writing – review & editing, Visualization. **Heta Lampinen:** Investigation, Visualization, Writing – review & editing. **Leah Lynham:** Writing – review & editing. **Nathan Reid:** Writing – review & editing. **Robert Thorne:** Writing – review & editing. **Mario Iglesias-Martínez:** Writing – review & editing. **Joël Brugger:** Writing – review & editing, Funding acquisition, Supervision. **Brad Cribb:** Resources, Investigation, Writing – review & editing. **Brett Hazelden:** Resources, Investigation, Funding acquisition. **Fang Xia:** Resources, Writing – review & editing.

Declaration of competing interest

The authors declare that they have no known competing financial interests or personal relationships that could have appeared to influence the work reported in this paper.

Acknowledgements

T.G.B. acknowledges financial support from an ARC-funded stipend scholarship, an International Tuition Fee Scholarship from Murdoch University, and a top-up scholarship from CSIRO. OD6 Metals (including CEO Dr. Darren Holden) are also acknowledged for providing access to company datasets and for partially funding the work.

Appendix A. Supplementary data

Supplementary data to this article can be found online at https://doi.org/10.1016/j.oregeorev.2025.106634.

Data availability

Data will be made available on request.

References

Aitchison, J., 1982. The statistical analysis of compositional data. J. R. Stat. Soc. Ser. B Stat. Methodol. 44, 139–160. https://doi.org/10.1111/j.2517-6161.1982.tb01195.x.

Anand, R.R., 2016. Regolith-landform processes and geochemical exploration for base metal deposits in regolith-dominated terrains of the Mt Isa region, northwest Queensland, Australia. Ore Geol. Rev. 73, 451–474. https://doi.org/10.1016/j.oregeorev.2015.08.014.

Anand, R.R., Butt, C.R.M., 2010. A guide for mineral exploration through the regolith in the Yilgarn Craton, Western Australia. Aust. J. Earth Sci. 57, 1015–1114. https://doi.org/10.1080/08120099.2010.522823.

Anand, R.R., Paine, M., 2002. Regolith geology of the Yilgarn Craton, Western Australia: implications for exploration. Aust. J. Earth Sci. 49, 3–162. https://doi.org/10.1046/j.1440-0952.2002.00912.x.

Anenburg, M., Williams, M.J., 2022. Quantifying the tetrad effect, shape components, and Ce–Eu–Gd anomalies in rare earth element patterns. Math. Geosci. 54, 47–70. https://doi.org/10.1007/s11004-021-09959-5.

Arhin, E., Zango, S.M., 2015. Unravelling regolith material types using Mg/Al and K/Al plot to support field regolith identification in the savannah regions of NW Ghana, West Africa. J. Afr. Earth Sc. 112, 597–607. https://doi.org/10.1016/j.jafrearsci.2015.09.007.

Aubert, D., Stille, P., Probst, A., 2001. REE fractionation during granite weathering and removal by waters and suspended loads: Sr and Nd isotopic evidence. Geochim. Cosmochim. Acta 65, 387–406. https://doi.org/10.1016/S0016-7037(00)00546-9.

Balaram, V., 2019. Rare earth elements: a review of applications, occurrence, exploration, analysis, recycling, and environmental impact. Geosci. Front. 10, 1285–1303. https://doi.org/10.1016/j.gsf.2018.12.005.

Bamforth, T.G., Hu, S., González-Álvarez, I., 2022. Developing geochemical exploration vectors through principal component analysis: a users guide by case study of the Woodlawn volcanogenic massive sulfide deposit, NSW. https://doi.org/10.25919/0xjn-wq15.

Bamforth, T.G., Xia, F., Putnis, A., Brugger, J., Hu, S.-Y., Roberts, M.P., Suvorova, A., Pring, A., 2024a. Hydrothermal mineral replacement in the apatite-rhabdophane-monazite system: experiments, reaction mechanisms and geological implications. Chem. Geol. 666, 122307. https://doi.org/10.1016/j.chemgeo.2024.122307.

Bamforth, T.G., Xia, F., Tiddy, C.J., González-Álvarez, I., Brugger, J., Hu, S.-Y., Schoneveld, L.E., Pearce, M.A., Putnis, A., 2024b. High-Grade REE accumulation in regolith: insights from supergene alteration of an apatite-rich vein at the Kapunda Cu mine, South Australia. Miner. Depos. 59, 1479–1503. https://doi.org/10.1007/s00126-024-01283-2.

Bao, Z., Zhao, Z., 2008. Geochemistry of mineralization with exchangeable REY in the weathering crusts of granitic rocks in South China. Ore Geol. Rev. 33, 519–535. https://doi.org/10.1016/j.oregeorev.2007.03.005.

Barrat, J.-A., Bayon, G., Lalonde, S., 2023. Calculation of cerium and lanthanum anomalies in geological and environmental samples. Chem. Geol. 615, 121202. https://doi.org/10.1016/j.chemgeo.2022.121202.

Belogub, E.V., Shilovskikh, V.V., Novoselov, K.A., Blinov, I.A., Filippova, K.A., 2021. Authigenic rhabdophane from brown iron ore of the oxidation zone of the Babaryk massive sulfide occurrence (South Urals): scanning electron microscope (SEM) and electron backscattered diffraction (EBSD) study. Eur. J. Mineral. 33, 605–620. https://doi.org/10.5194/ejm-33-605-2021.

Berger, A., Janots, E., Gnos, E., Frei, R., Bernier, F., 2014. Rare earth element mineralogy and geochemistry in a laterite profile from Madagascar. Appl. Geochem. 41, 218–228. https://doi.org/10.1016/j.apgeochem.2013.12.013.

Berman, M., Bischof, L., Lagerstrom, R., Guo, Y., Huntington, J., Mason, P., Green, A.A., 2017. A comparison between three sparse unmixing algorithms using a large library of shortwave infrared mineral spectra. IEEE Trans. Geosci. Remote Sens. 55, 3588–3610. https://doi.org/10.1109/TGRS.2017.2676816.

Berner, R.A., 1985. Sulphate reduction, organic matter decomposition and pyrite formation. Philos. Trans. R. Soc. London Ser. A 315, 25–38. https://doi.org/10.1098/rsta.1985.0027.

Berner, R.A., 1984. Sedimentary pyrite formation: an update. Geochim. Cosmochim. Acta 48, 605–615. https://doi.org/10.1016/0016-7037(84)90089-9.
Berner, R.A., Westrich, J.T., 1985. Bioturbation and the early diagenesis of carbon and sulfur. Am. J. Sci. 285, 193–206. https://doi.org/10.2475/ajs.285.3.193.
Braun, J.-J., Pagel, M., Muller, J.-P., Bilong, P., Michard, A., Guillet, B., 1990. Cerium anomalies in lateritic profiles. Geochim. Cosmochim. Acta 54, 781–795. https://doi.org/10.1016/0016-7037(90)90373-S.
Butt, C.R.M., 2016. The development of regolith exploration geochemistry in the tropics and sub-tropics. Ore Geol. Rev. 73, 380–393. https://doi.org/10.1016/j.oregeorev.2015.08.018.
Butt, C.R.M., Lintern, M.J., Anand, R.R., 2000. Evolution of regoliths and landscapes in deeply weathered terrain—implications for geochemical exploration. Ore Geol. Rev. 16, 167–183. https://doi.org/10.1016/S0169-1368(99)00029-3.
Carpenter, R., Pole, M., 1995. Eocene plant fossils from the Lefroy and Cowan paleodrainages, Western Australia. Aust. Syst. Bot. 8, 1107. https://doi.org/10.1071/SB9951107.
Carranza, E.J.M., 2011. Analysis and mapping of geochemical anomalies using logratio-transformed stream sediment data with censored values. J. Geochem. Explor. 110, 167–185. https://doi.org/10.1016/j.gexplo.2011.05.007.
Caruso, A.S., Clarke, K.D., Tiddy, C.J., Delean, S., Lewis, M.M., 2018. Objective regolith-landform mapping in a regolith dominated terrain to inform mineral exploration. Geosciences (basel) 8, 318. https://doi.org/10.3390/geosciences8090318.
Clarke, J.D.A., 1994. Evolution of the Lefroy and Cowan palaeodrainage channels, Western Australia. Aust. J. Earth Sci. 41, 55–68. https://doi.org/10.1080/08120099408728113.
Clarke, J.D.A., Gammon, P.R., Hou, B., Gallagher, S.J., 2003. Middle to Upper Eocene stratigraphic nomenclature and deposition in the Eucla Basin. Aust. J. Earth Sci. 50, 231–248. https://doi.org/10.1046/j.1440-0952.2003.00995.x.
Condie, K.C., Dengate, J., Cullers, R.L., 1995. Behavior of rare earth elements in a paleoweathering profile on granodiorite in the Front Range, Colorado, USA. Geochim. Cosmochim. Acta 59, 279–294. https://doi.org/10.1016/0016-7037(94)00280-Y.
de Broekert, P., Sandiford, M., 2005. Buried inset-valleys in the Eastern Yilgarn Craton, Western Australia: geomorphology, age, and allogenic control. J. Geol. 113, 471–493. https://doi.org/10.1086/430244.
de Caritat, P., Main, P.T., Grunsky, E.C., Mann, A.W., 2017. Recognition of geochemical footprints of mineral systems in the regolith at regional to continental scales. Aust. J. Earth Sci. 64, 1033–1043. https://doi.org/10.1080/08120099.2017.1259184.
De Silva, J., Smith, R.A., 2010. Significance of paleovalley sediments and landscape in the development of stream salinity in three southwest Australian catchments. Aust. J. Earth Sci. 57, 221–230. https://doi.org/10.1080/08120090903521689.
Dormann, C.F., Elith, J., Bacher, S., Buchmann, C., Carl, G., Carré, G., Marquéz, J.R.G., Gruber, B., Lafourcade, B., Leitão, P.J., Münkemüller, T., McClean, C., Osborne, P.E., Reineking, B., Schröder, B., Skidmore, A.K., Zurell, D., Lautenbach, S., 2013. Collinearity: a review of methods to deal with it and a simulation study evaluating their performance. Ecography 36, 27–46. https://doi.org/10.1111/j.1600-0587.2012.07348.x.
Doublier, M.P., Roache, T., Potel, S., 2010. Short-wavelength infrared spectroscopy: a new petrological tool in low-grade to very low-grade pelites. Geology 38, 1031–1034. https://doi.org/10.1130/G31272.1.
Eggleton, R.A., 2001. The regolith glossary, in: Surficial Geology, Soils, and Landscapes. Cooperative Research Centre for Landscape Evolution and Mineral Exploration.
Embleton, B.J.J., 1981. A review of the paleomagnetism of Australia and Antarctica. pp. 77–92. https://doi.org/10.1029/GD002p0077.
Eyles, N., de Broekert, P., 2001. Glacial tunnel valleys in the Eastern Goldfields of Western Australia cut below the Late Paleozoic Pilbara ice sheet. Palaeogeogr. Palaeoclimatol. Palaeoecol. 171, 29–40. https://doi.org/10.1016/S0031-0182(01)00265-6.
Fandeur, D., Juillot, F., Morin, G., Olivi, L., Cognigni, A., Webb, S.M., Ambrosi, J.-P., Fritsch, E., Guyot, F., Brown Jr., G.E., 2009. XANES evidence for oxidation of Cr(III) to Cr(VI) by Mn-oxides in a lateritic regolith developed on serpentinized ultramafic rocks of New Caledonia. Environ. Sci. Tech. 43, 7384–7390. https://doi.org/10.1021/es900498r.
Filzmoser, P., Hron, K., Reimann, C., 2009. Principal component analysis for compositional data with outliers. Environmetrics 20, 621–632. https://doi.org/10.1002/env.966.
Fu, W., Li, X., Feng, Y., Feng, M., Peng, Z., Yu, H., Lin, H., 2019. Chemical weathering of S-type granite and formation of Rare Earth Element (REE)-rich regolith in South China: critical control of lithology. Chem. Geol. 520, 33–51. https://doi.org/10.1016/j.chemgeo.2019.05.006.
Gall, Q., 1994. The proterozoic thelon paleosol, Northwest Territories, Canada. Precambr. Res. 68, 115–137. https://doi.org/10.1016/0301-9268(94)90068-X.
Gammon, P.R., James, N.P., Clarke, J.D.A., Bone, Y., 2000. Sedimentology and lithostratigraphy of Upper Eocene sponge-rich sediments, southern Western Australia. Aust. J. Earth Sci. 47, 1087–1103. https://doi.org/10.1046/j.1440-0952.2000.00835.x.
García, M., Maksaev, V., Townley, B., Dilles, J., 2017. Metallogeny, structural evolution, post-mineral cover distribution and exploration in concealed areas of the northern Chilean Andes. Ore Geol. Rev. 86, 652–672. https://doi.org/10.1016/j.oregeorev.2017.01.025.
Gong, Q., Deng, J., Wang, C., Wang, Z., Zhou, L., 2013. Element behaviors due to rock weathering and its implication to geochemical anomaly recognition: a case study on Linglong biotite granite in Jiaodong peninsula, China. J. Geochem. Explor. 128, 14–24. https://doi.org/10.1016/j.gexplo.2013.01.004.
González-Álvarez, I., Boni, M., Anand, R.R., 2016a. Mineral exploration in regolith-dominated terrains: global considerations and challenges. Ore Geol. Rev. 73, 375–379. https://doi.org/10.1016/j.oregeorev.2015.11.017.
González-Álvarez, I., Goncalves, M.A., Carranza, E.J.M., 2020. Introduction to the Special Issue Challenges for mineral exploration in the 21st century: Targeting mineral deposits under cover. Ore Geol Rev 126, 103785. https://doi.org/10.1016/j.oregeorev.2020.103785.
González-Álvarez, I., Salama, W., Anand, R.R., 2016b. Sea-level changes and buried islands in a complex coastal palaeolandscape in the South of Western Australia: implications for greenfield mineral exploration. Ore Geol. Rev. 73, 475–499. https://doi.org/10.1016/j.oregeorev.2015.10.002.
Haest, M., Cudahy, T., Laukamp, C., Gregory, S., 2012a. Quantitative mineralogy from infrared spectroscopic data. II. Three-dimensional mineralogical characterization of the Rocklea channel Iron Deposit, Western Australia. Econ. Geol. 107, 229–249. https://doi.org/10.2113/econgeo.107.2.229.
Haest, M., Cudahy, T., Laukamp, C., Gregory, S., 2012b. Quantitative mineralogy from infrared spectroscopic data. I. Validation of mineral abundance and composition scripts at the Rocklea Channel Iron Deposit in Western Australia. Econ. Geol. 107, 209–228. https://doi.org/10.2113/econgeo.107.2.209.
Henne, A., Craw, D., Gagen, E.J., Southam, G., 2019. Bacterially-mediated supergene alteration and redistribution of copper in mineralised rocks at the Salobo IOCG deposit, Brazil. Ore Geol. Rev. 115, 103210. https://doi.org/10.1016/j.oregeorev.2019.103210.
Hood, S.B., Cracknell, M.J., Gazley, M.F., Reading, A.M., 2019. Element mobility and spatial zonation associated with the Archean Hamlet orogenic Au deposit, Western Australia: implications for fluid pathways in shear zones. Chem. Geol. 514, 10–26. https://doi.org/10.1016/j.chemgeo.2019.03.022.
Ichimura, K., Sanematsu, K., Kon, Y., Takagi, T., Murakami, T., 2020. REE redistributions during granite weathering: Implications for Ce anomaly as a proxy for paleoredox states. Am. Mineral. 105, 848–859. https://doi.org/10.2138/am-2020-7148.
Itzstein-Davey, F., 2004. A spatial and temporal Eocene palaeoenvironmental study, focusing on the Proteaceae family, from Kambalda, Western Australia. Rev. Palaeobot. Palynol. 131, 159–180. https://doi.org/10.1016/j.revpalbo.2004.03.008.
Jeong, G.Y., 2000. The dependence of localized crystallization of halloysite and kaolinite on primary minerals in the weathering profile of granite. Clays Clay Miner. 48, 196–203. https://doi.org/10.1346/CCMN.2000.0480205.
Johnson, C.B., McQueen, K.G., 2001. The nature of gold-bearing palaeochannel sediments in the Gidji area north of Kalgoorlie, Western Australia. Quat. Int. 82, 51–62. https://doi.org/10.1016/S1040-6182(01)00008-8.
Jowitt, S.M., Wong, V.N.L., Wilson, S., Gore, O., 2017. Critical metals in the critical zone: controls, resources and future prospectivity of regolith-hosted rare earth elements. Aust. J. Earth Sci. 64, 1045–1054. https://doi.org/10.1080/08120099.2017.1380701.
Kalinin, Y.A., Palyanova, G.A., Naumov, E.A., Kovalev, K.R., Pirajno, F., 2019. Supergene remobilization of Au in Au-bearing regolith related to orogenic deposits: a case study from Kazakhstan. Ore Geol. Rev. 109, 358–369. https://doi.org/10.1016/j.oregeorev.2019.04.019.
Kalintsev, A., Brugger, J., Etschmann, B., Ram, R., 2021. An *in situ*, micro-scale investigation of inorganically and organically driven rare-earth remobilisation during weathering. Mineral. Mag. 85, 105–116. https://doi.org/10.1180/mgm.2021.4.
Kelka, U., Martinez, C., Krapf, C., Westerlund, S., Gonzalez-Alvarez, I., Pawley, M., Foss, C., 2022. Establishing an integrated workflow identifying and linking surface and subsurface lineaments for mineral exploration under cover: example from the Gawler Craton, South Australia. Solid Earth 13, 827–847. https://doi.org/10.5194/se-13-827-2022.
Kirkland, C.L., Smithies, R.H., Spaggiari, C.V., 2015. Foreign contemporaries – unravelling disparate isotopic signatures from Mesoproterozoic Central and Western Australia. Precambr. Res. 265, 218–231. https://doi.org/10.1016/j.precamres.2014.12.001.
Kirkland, C.L., Spaggiari, C.V., Pawley, M.J., Wingate, M.T.D., Smithies, R.H., Howard, H.M., Tyler, I.M., Belousova, E.A., Poujol, M., 2011. On the edge: U–Pb, Lu–Hf, and Sm–Nd data suggests reworking of the Yilgarn craton margin during formation of the Albany-Fraser Orogen. Precambr. Res. 187, 223–247. https://doi.org/10.1016/j.precamres.2011.03.002.
Krzanowski, W.J., Lai, Y.T., 1988. A criterion for determining the number of groups in a data set using sum-of-squares clustering. Biometrics 44, 23. https://doi.org/10.2307/2531893.
Laukamp, C., Rodger, A., LeGras, M., Lampinen, H., Lau, I.C., Pejcic, B., Stromberg, J., Francis, N., Ramanaidou, E., 2021. Mineral physicochemistry underlying feature-based extraction of mineral abundance and composition from shortwave, mid and thermal infrared reflectance spectra. Minerals 11, 347. https://doi.org/10.3390/min11040347.
Laukamp, C., Salama, W., González-Álvarez, I., 2016. Proximal and remote spectroscopic characterisation of regolith in the Albany–Fraser Orogen (Western Australia). Ore Geol. Rev. 73, 540–554. https://doi.org/10.1016/j.oregeorev.2015.10.003.
Li, Y.H.M., Zhao, W.W., Zhou, M.-F., 2017. Nature of parent rocks, mineralization styles and ore genesis of regolith-hosted REE deposits in South China: an integrated genetic model. J. Asian Earth Sci. 148, 65–95. https://doi.org/10.1016/j.jseaes.2017.08.004.
Lin, X., Wang, X., Zhang, B., Yao, W., 2014. Multivariate analysis of regolith sediment geochemical data from the Jinwozi gold field, north-western China. J. Geochem. Explor. 137, 48–54. https://doi.org/10.1016/j.gexplo.2013.11.006.
Liu, W., Li, Y., Wang, X., Cui, L., Zhao, Z., Liu, C., Xu, Z., 2022. Weathering stage and topographic control on rare earth element (REE) behavior: new constraints from a

deeply weathered granite hill. Chem. Geol. 610, 121066. https://doi.org/10.1016/j.chemgeo.2022.121066.
Liu, W., Liu, C., Brantley, S.L., Xu, Z., Zhao, T., Liu, T., Yu, C., Xue, D., Zhao, Z., Cui, L., Zhang, Z., Fan, B., Gu, X., 2016. Deep weathering along a granite ridgeline in a subtropical climate. Chem. Geol. 427, 17–34. https://doi.org/10.1016/j.chemgeo.2016.02.014.
Löhr, S.C., Spandler, C., Baldermann, A., 2024. Controls on rapid rare earth element enrichment in sediments deposited by a continental-scale river system. Geochim. Cosmochim. Acta 366, 48–64. https://doi.org/10.1016/j.gca.2023.12.012.
Metelka, V., Baratoux, L., Jessell, M.W., Barth, A., Ježek, J., Naba, S., 2018. Automated regolith landform mapping using airborne geophysics and remote sensing data, Burkina Faso, West Africa. Remote Sens. Environ. 204, 964–978. https://doi.org/10.1016/j.rse.2017.08.004.
Middelburg, J.J., van der Weijden, C.H., Woittiez, J.R.W., 1988. Chemical processes affecting the mobility of major, minor and trace elements during weathering of granitic rocks. Chem. Geol. 68, 253–273. https://doi.org/10.1016/0009-2541(88)90025-3.
Mingyuan, H., 1992. Distribution characteristics of the weathering crust-type rare earth resources in Nanling, China. J. Nat. Resour. 7, 64–70. https://doi.org/10.11849/zrzyxb.1992.01.008.
Mory, A.J., Redfern, J., Martin, J.R., 2008. A review of Permian–Carboniferous glacial deposits in Western Australia, in: Special Paper 441: Resolving the Late Paleozoic Ice Age in Time and Space. Geological Society of America, pp. 29–40. https://doi.org/10.1130/2008.2441(02).
Nesbitt, H.W., 1979. Mobility and fractionation of rare earth elements during weathering of a granodiorite. Nature 279, 206–210. https://doi.org/10.1038/279206a0.
Nesbitt, H.W., Young, G.M., 1982. Early Proterozoic climates and plate motions inferred from major element chemistry of lutites. Nature 299, 715–717. https://doi.org/10.1038/299715a0.
O'Neill, H., St, C., 2016. The smoothness and shapes of chondrite-normalized rare earth element patterns in basalts. J. Petrol. 57, 1463–1508. https://doi.org/10.1093/petrology/egw047.
Papoulis, D., Tsolis-Katagas, P., Katagas, C., 2004. Progressive stages in the formation of kaolin minerals of different morphologies in the weathering of plagioclase. Clays Clay Miner. 52, 275–286. https://doi.org/10.1346/CCMN.2004.0520303.
Pillans, B., 2005. Geochronology of the Australian regolith. In: Anand, R.R., de Broekert, P. (Eds.), Regolith Landscape Evolution across Australia: A Compilation of Regolith Landscape Case Studies with Regolith Landscape Evolution Models. CRC Leme, pp. 41–61.
Price, J.R., Velbel, M.A., 2003. Chemical weathering indices applied to weathering profiles developed on heterogeneous felsic metamorphic parent rocks. Chem. Geol. 202, 397–416. https://doi.org/10.1016/j.chemgeo.2002.11.001.
Ram, R., Becker, M., Brugger, J., Etschmann, B., Burcher-Jones, C., Howard, D., Kooyman, P.J., Petersen, J., 2019. Characterisation of a rare earth element- and zirconium-bearing ion-adsorption clay deposit in Madagascar. Chem. Geol. 522, 93–107. https://doi.org/10.1016/j.chemgeo.2019.05.011.
Richardson, J.B., King, E.K., 2018. Regolith Weathering and Sorption Influences Molybdenum, Vanadium, and Chromium Export via Stream Water at Four Granitoid Critical Zone Observatories. Front Earth Sci (lausanne) 6. https://doi.org/10.3389/feart.2018.00193.
Robertson, I.D.M., Eggleton, R.A., 1991. Weathering of Granitic Muscovite to Kaolinite and Halloysite and of Plagioclase-Derived Kaolinite to Halloysite. Clays Clay Miner. 39, 113–126. https://doi.org/10.1346/CCMN.1991.0390201.
Sababa, E., Essomba Owona, L.G., Temga, J.P., Ndjigui, P.-D., 2021. Petrology of weathering materials developed on granites in Biou area, North-Cameroon: implication for rare-earth elements (REE) exploration in semi-arid regions. Heliyon 7, e08581. https://doi.org/10.1016/j.heliyon.2021.e08581.
Salama, W., Anand, R.R., 2017. Reconstructing the pre-Quaternary landscape in Agnew–Lawlers area, Western Australia with emphasis on the Permo-Carboniferous glaciation and post-glacial weathering. Int. J. Earth Sci. 106, 311–339. https://doi.org/10.1007/s00531-016-1320-5.
Salama, W., Anand, R.R., Verrall, M., 2016a. Mineral exploration and basement mapping in areas of deep transported cover using indicator heavy minerals and paleoredox fronts, Yilgarn Craton, Western Australia. Ore Geol. Rev. 72, 485–509. https://doi.org/10.1016/j.oregeorev.2015.07.014.
Salama, W., González-Álvarez, I., Anand, R.R., 2016b. Significance of weathering and regolith/landscape evolution for mineral exploration in the NE Albany-Fraser Orogen, Western Australia. Ore Geol. Rev. 73, 500–521. https://doi.org/10.1016/j.oregeorev.2015.07.024.
Sanematsu, K., Kon, Y., Imai, A., 2015. Influence of phosphate on mobility and adsorption of REEs during weathering of granites in Thailand. J. Asian Earth Sci. 111, 14–30. https://doi.org/10.1016/j.jseaes.2015.05.018.
Sanematsu, K., Kon, Y., Imai, A., Watanabe, K., Watanabe, Y., 2013. Geochemical and mineralogical characteristics of ion-adsorption type REE mineralization in Phuket, Thailand. Miner Depos 48, 437–451. https://doi.org/10.1007/s00126-011-0380-5.
Sanematsu, K., Watanabe, Y., 2016. Characteristics and Genesis of Ion Adsorption-Type Rare Earth Element Deposits, in: Rare Earth and Critical Elements in Ore Deposits. Society of Economic Geologists. https://doi.org/10.5382/Rev.18.03.
Santana, I.V., Botelho, N.F., 2022. REE residence, behaviour and recovery from a weathering profile related to the Serra Dourada Granite, Goiás/Tocantins States, Brazil. Ore Geol. Rev. 143, 104751. https://doi.org/10.1016/j.oregeorev.2022.104751.
Schodlok, M.C., Whitbourn, L., Huntington, J., Mason, P., Green, A., Berman, M., Coward, D., Connor, P., Wright, W., Jolivet, M., Martinez, R., 2016. HyLogger-3, a visible to shortwave and thermal infrared reflectance spectrometer system for drill core logging: functional description. Aust. J. Earth Sci. 63. https://doi.org/10.1080/08120099.2016.1231133.
Schwertmann, U., Pfab, G., 1996. Structural vanadium and chromium in lateritic iron oxides: Genetic implications. Geochim. Cosmochim. Acta 60, 4279–4283. https://doi.org/10.1016/S0016-7037(96)00259-1.
Sergeev, N., Collins, T., 2024. Regolith-hosted rare earth element mineralization in the Esperance Region, Western Australia: major characteristics and potential controls. Minerals 14, 847. https://doi.org/10.3390/min14080847.
Smith, N.R.A., Reading, A.M., Asten, M.W., Funk, C.W., 2013. Constraining depth to basement for mineral exploration using microtremor: a demonstration study from remote inland Australia. Geophysics 78, B227–B242. https://doi.org/10.1190/geo2012-0449.1.
Smithies, R., Spaggiari, C., Kirkland, C., 2015. Building the crust of the Albany-Fraser Orogen; constraints from granite geochemistry. Geol. Survey Western Australia Report 150, 49.
Sonntag, I., Laukamp, C., Hagemann, S.G., 2012. Low potassium hydrothermal alteration in low sulfidation epithermal systems as detected by IRS and XRD: an example from the Co–O mine, Eastern Mindanao, Philippines. Ore Geol. Rev. 45, 47–60. https://doi.org/10.1016/j.oregeorev.2011.08.001.
Thió-Henestrosa, S., Martín-Fernández, J.A., 2005. Dealing with compositional data: the freeware CoDaPack. Math. Geol. 37, 773–793. https://doi.org/10.1007/s11004-005-7379-3.
Trench, A., Zhang, L., Groves, D.I., Crook, D., Brand, N.W., 2024. Australian critical metal exploration for analogues of Chinese ionic-clay REE deposits. Geosyst. Geoenviron., 100293 https://doi.org/10.1016/j.geogeo.2024.100293.
Tsuzuki, Y., Kawabe, I., 1983. Polymorphic transformations of kaolin minerals in aqueous solutions. Geochim. Cosmochim. Acta 47, 59–66. https://doi.org/10.1016/0016-7037(83)90090-X.
Ugwu, I.M., Sherman, D.M., 2019. The solubility of goethite with structurally incorporated nickel and cobalt: Implication for laterites. Chem. Geol. 518, 1–8. https://doi.org/10.1016/j.chemgeo.2019.04.021.
Van de Graaff, W.J.E., Crowe, R.W.A., Bunting, J.A., Jackson, M.J., 1977. Relict early cainozoic drainages in arid Western Australia. Zeitschrift Für Geomorphologie 21, 379–400. https://doi.org/10.1127/zfg/21/1977/379.
Wilford, J.R., Searle, R., Thomas, M., Pagendam, D., Grundy, M.J., 2016. A regolith depth map of the Australian continent. Geoderma 266, 1–13. https://doi.org/10.1016/j.geoderma.2015.11.033.
Worrall, L., Munday, T., Green, A., 1998. Beyond bump finding – airborne electromagnetics for mineral exploration in regolith dominated terrains. Explor. Geophys. 29, 199–203. https://doi.org/10.1071/EG998199.
Wang, X., Zhang, B., Lin, X., Xu, S., Yao, W., Ye, R., 2016. Geochemical challenges of diverse regolith-covered terrains for mineral exploration in China. Ore Geol. Rev. 73, 417–431. https://doi.org/10.1016/j.oregeorev.2015.08.015.
Yang, M., Liang, X., Ma, L., Huang, J., He, H., Zhu, J., 2019. Adsorption of REEs on kaolinite and halloysite: a link to the REE distribution on clays in the weathering crust of granite. Chem. Geol. 525, 210–217. https://doi.org/10.1016/j.chemgeo.2019.07.024.
Yusoff, Z.M., Ngwenya, B.T., Parsons, I., 2013. Mobility and fractionation of REEs during deep weathering of geochemically contrasting granites in a tropical setting, Malaysia. Chem. Geol. 349–350, 71–86. https://doi.org/10.1016/j.chemgeo.2013.04.016.
Zhou, X., Li, A., Jiang, F., Lu, J., 2015. Effects of grain size distribution on mineralogical and chemical compositions: a case study from size-fractional sediments of the Huanghe (Yellow River) and Changjiang (Yangtze River). Geol. J. 50, 414–433. https://doi.org/10.1002/gj.2546.
Zuoping, Z., Chuanxian, L., 1996. The behaviour of rare-earth elements (REE) during weathering of granites in southern Guangxi, China. Chin. J. Geochem. 15, 344–352. https://doi.org/10.1007/BF02867008.